

Lithospheric bending at subduction zones based on depth soundings and satellite gravity

Daniel A. Levitt and David T. Sandwell

Scripps Institution of Oceanography, La Jolla, California

Abstract. A global study of trench flexure was performed by simultaneously modeling 117 bathymetric profiles (original depth soundings) and satellite-derived gravity profiles. A thin, elastic plate flexure model was fit to each bathymetry/gravity profile by minimization of the L_1 norm. The six model parameters were regional depth, regional gravity, trench axis location, flexural wavelength, flexural amplitude, and lithospheric density. A regional tilt parameter was not required after correcting for age-related trend using a new high-resolution age map. Estimates of the density parameter confirm that most outer rises are uncompensated. We find that flexural wavelength is not an accurate estimate of plate thickness because of the high curvatures observed at a majority of trenches. As in previous studies, we find that the gravity data favor a longer-wavelength flexure than the bathymetry data. A joint topography-gravity modeling scheme and fit criteria are used to limit acceptable parameter values to models for which topography and gravity yield consistent results. Even after the elastic thicknesses are converted to mechanical thicknesses using the yield strength envelope model, residual scatter obscures the systematic increase of mechanical thickness with age; perhaps this reflects the combination of uncertainties inherent in estimating flexural wavelength, such as extreme inelastic bending and accumulated thermoelastic stress. The bending moment needed to support the trench and outer rise topography increases by a factor of 10 as lithospheric age increases from 20 to 150 Ma; this reflects the increase in saturation bending moment that the lithosphere can maintain. Using a stiff, dry-olivine rheology, we find that the lithosphere of the GDH1 thermal model (Stein and Stein, 1992) is too hot and thin to maintain the observed bending moments. Moreover, the regional depth seaward of the oldest trenches (~150 Ma) exceeds the GDH1 model depths by about 400 m.

Introduction

Analysis of the flexural response of the lithosphere to loading at seamounts, trenches and fracture zones has provided estimates of the mechanical thickness (h_m) of oceanic lithosphere as a function of age, generally confirming an age-thickening relationship [Watts, 1978; Caldwell and Turcotte, 1979] in accordance with lithospheric cooling models [Turcotte and Oxburgh, 1967; McKenzie, 1967; Parsons and Sclater, 1977]. The base of the mechanical lithosphere, defined as the depth to which deviatoric stress can be maintained over geological timescales, is believed to correspond to a specific isotherm. Estimates of mechanical thickness have been obtained by modeling flexural behavior as elastic [Turcotte, 1979], as elastic-plastic with constant yield strength [McAdoo et al., 1978], as elastic-plastic with variable yield strength [Goetze and Evans, 1979] and as viscous [DeBremaecker, 1977]. Presently, models employing elastic and elastic-plastic theory are preferred, though horizontal stress components are often deemed necessary in order to optimally reduce data misfit [Parsons and Molnar, 1976; McQueen and Lambeck, 1989]. In order to keep the data analysis simple, the classic approach estimates the thickness of a thin elastic plate (h_e) that approximates the flexural

behavior of the real lithosphere [Gunn, 1943; Watts, 1978]. These elastic model parameters can then be used to establish the mechanical thickness (h_m) of an elastic-plastic lithosphere by assuming a given rheology [McNutt and Menard, 1982; McNutt, 1984] or lithospheric viscosity [DeBremaecker, 1977].

At many trenches the large curvatures of the flexed lithosphere cause brittle fracture of the upper lithosphere and ductile flow of the lower lithosphere so that the estimated elastic thickness is much less than the true mechanical thickness; at seamounts, smaller curvatures result in less fracture and flow so that h_e is a good approximation of h_m . Following the method of McNutt and Menard [1982], true mechanical thickness values can be estimated based on the elastic thickness and curvature. Nevertheless, the current database of thickness estimates displays a distinct bimodality between h_m values deduced at seamounts and trenches [Wessel, 1992]. One possible explanation of this is that thermal bending stress due to cooling of the lithosphere with age can prestress the flat-lying plate so that when it is bent concave downward (trench) it appears stronger than when it is bent concave upward (seamount) [Wessel, 1992].

Present published results concerning trench flexure have been obtained from a composite of mixed data sources (topography, geoid, and gravity) as well as a variety of analytical techniques. Having limited computer power, Caldwell et al. [1976], Caldwell and Turcotte [1979], Jones et al. [1978], and Turcotte et al. [1978] determined elastic thickness for topographic profiles by measuring the distance

Copyright 1995 by the American Geophysical Union.

Paper number 94JB02468.
0148-0227/95/94JB-02468\$05.00

between the first zero crossing and the outer rise peak x_b after arbitrarily assigning a baseline local depth. *McNutt* [1984] utilized a similar technique on topographic profiles generated from contour maps. *Bodine and Watts* [1979] did not estimate elastic thickness but assumed the base of the elastic layer was defined by the 500°C isotherm; they then varied the amplitude of the flexure w_b to best match eight topographic profiles. *McAdoo et al.* [1978] fitted topographic and gravity profiles to model-generated flexural deflection curves. *McAdoo and Martin* [1984] and *McAdoo et al.* [1985] generated estimates of flexural wavelength α and w_b from an ensemble of Seasat geoid observations. *Carey and Dubois* [1981] used a finite element method with specific point determination on topographic and seismic data. *Judge and McNutt* [1991] utilized a composite topography-geoid-gravity database to estimate the elastic thickness and plate curvatures at the Peru and Chile Trenches. A potential problem with their analysis is the use of highly interpolated topographic profiles where the interpolation algorithm uses thin, elastic plate flexure theory to fill the gaps [Smith, 1993]. *McQueen and Lambeck* [1989] fitted thin, elastic plate flexure models to 14 topographic profiles across the major western Pacific trenches where they specifically included model parameters for regional depth, regional slope, and first zero crossing location. By simultaneously minimizing these parameters along with the standard flexural parameters, they found a very wide range of acceptable models and suggested that estimates of elastic thickness from all previous studies are very uncertain.

The purpose of this study is to perform a uniform, unbiased analysis of global trench flexure by using original bathymetric soundings combined with a newly constructed global gravity grid derived from ERS 1, Geosat, and Seasat

altimetry data [Sandwell and Smith, 1992]. Trench outer rise profiles are obtained from a global database of original geophysical data [Smith, 1993]. Many (117) profiles are selected in an effort to sample a range of relevant parameters such as lithospheric age, geographic location, subduction rate, slab dip, and slab depth (Figure 1). In order to maximize data quality and consistency, profiles are located in close proximity to long, approximately trench-normal bathymetric tracks. Free air gravity anomalies are extracted from a global grid of satellite altimetry data [Sandwell and Smith, 1992] along the topographic profiles. We simultaneously model trench outer rise topography and gravity using a thin elastic plate flexure model, but in contrast to previous studies, we also specifically include regional depth and first zero crossing position as model parameters. By using an improved seafloor age model [Roest et al., 1992] we are able to correct the topographic profiles for regional slope so that this parameter is not required. Later we interpret these results in terms of yield strength envelope models.

Stein and Stein [1992] have recently developed a model of a thinner, hotter lithosphere (GDH1) than the plate (PSM) and half-space (HS) models of *Parsons and Sclater* [1977] in an effort to explain depth/age and heat flow/age observations for old oceanic lithosphere. More than 50 of our flexure profiles cross old lithosphere (100-140 Ma), where the differences in the predictions of these models is greatest, thus allowing for discrimination between lithospheric thermal models on the basis of their respective predicted mechanical properties. We use the regional depth, the bending moment needed to support the outer rise, and the mechanical thickness obtained at these sites to place constraints on the asymptotic lithospheric thickness.

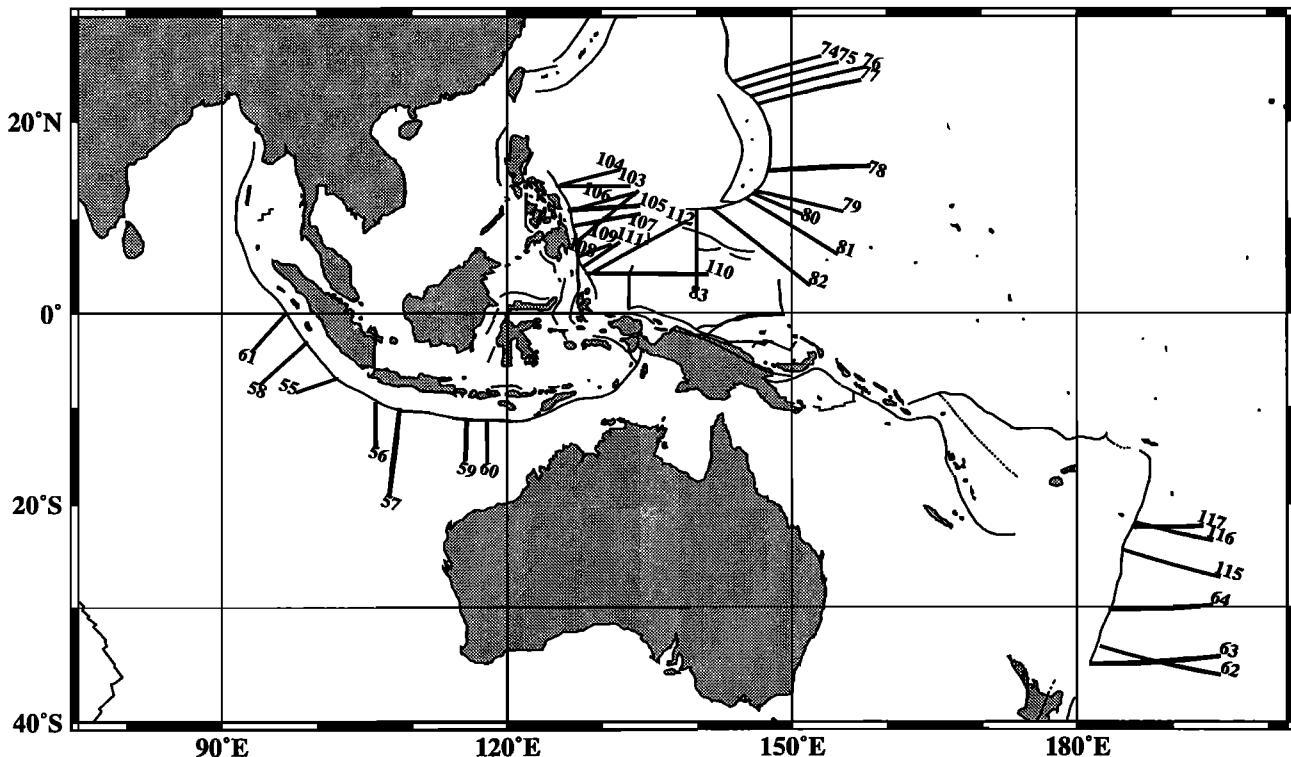


Figure 1a. Global great circle profile location map of Java, Kermadec, Marianas, Philippines, and Tonga Trenches. End points are presented in Table 1.

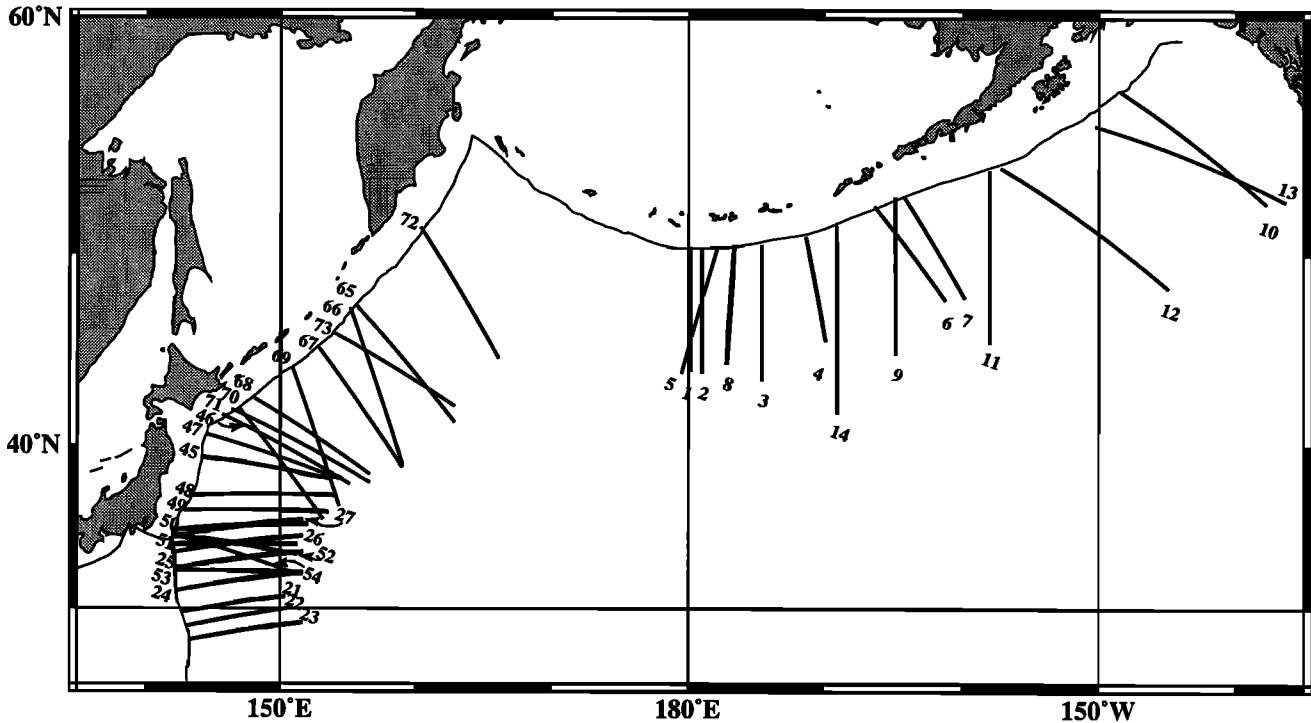


Figure 1b. Global great circle profile location map of Aleutians, Bonin, Japan, and Kuril Trenches. End points are presented in Table 1.

Flexure Model

In the elastic flexure model [Gunn, 1943; Watts, 1978], the thin plate is acted upon by a restoring force $g(\rho_m - \rho_w)w$, where w is the plate deflection, g is average gravity, and ρ_m and ρ_w are mantle and water density, respectively. If the applied load comprises a horizontal force P and a bending moment M the equilibrium equation is [Turcotte and Schubert, 1982]

$$\frac{d^2 M}{dx^2} + P \frac{d^2 w}{dx^2} - g(\rho_m - \rho_w)w = 0, \quad (1)$$

where the bending moment M is related to the negative curvature of the plate by the flexural rigidity D :

$$M = -D \frac{d^2 w}{dx^2}. \quad (2)$$

Parsons and Molnar [1976] demonstrate that the end load is only an important factor in modeling flexure profiles when it is a substantial fraction of the load required to buckle the lithosphere. Tectonic regimes landward of subduction zones do not show evidence for large compressive stress (~ 500 MPa) [Molnar and Atwater, 1978] and in many cases are sites of extension and spreading. Furthermore, S. Mueller and R. J. Phillips (unpublished manuscript, 1992) found, from synthetic profile analysis, that inplane stress regime cannot be reliably constrained by attempting to recover parameters from best fitting elastic profiles, even with respect to distinguishing between compression and tension. Therefore we do not include the end load as a parameter in our flexural modeling. Under these simplifications and assumptions, a model for the deflection of the plate in response to an applied bending moment M_o is

$$w(x) = w_o \exp\left[\frac{-(x - x_o)}{\alpha}\right] \sin\left[\frac{(x - x_o)}{\alpha}\right] + s(x - x_o) + d_o, \quad (3)$$

where w_o is the flexural amplitude parameter, x_o is the location of the load, s is the tilt parameter, d_o is the undeflected depth, and α is the flexural parameter (Figure 2). The flexural parameter is related to the elastic thickness h_e by

$$\alpha = \left[\frac{E h_e^3}{3(\rho_m - \rho_w)g(1 - \nu^2)} \right]^{1/4}, \quad (4)$$

where E is Young's modulus and ν is Poisson's ratio. Later we will show that the tilt parameter is not needed if the regional depth versus age relation is accounted for using an accurate age model.

In order to discriminate between uncompensated topographic variation due to flexure and unrelated topographic deflection, we utilize gravity profiles corresponding to the topographic profiles. Following McAdoo *et al.* [1978], a modified Bouguer approximation is used to determine gravity, and we include the approximate reduction in gravity amplitude due to upward continuation of a constant wavelength signal ($2\pi\alpha$) from the crust/water interface at a mean ocean depth of d_a as well as the mantle/crust interface at an additional crustal thickness depth h_c . The attenuated gravity anomaly amplitude is thus obtained by

$$\Delta g(x) = 2\pi G \rho_o w_o \exp\left[\frac{-(x - x_o)}{\alpha}\right] \sin\left[\frac{(x - x_o)}{\alpha}\right] \cdot \left\{ \left(\frac{\rho_c - \rho_w}{\rho_m - \rho_w} \right) \exp\left[\frac{-d_a}{\alpha}\right] + \left(\frac{\rho_m - \rho_c}{\rho_m - \rho_w} \right) \exp\left[\frac{-(d_a + h_c)}{\alpha}\right] \right\} + \Delta g_o \quad (5)$$

where G is the gravitational constant, Δg_o is the mean regional gravity anomaly, and ρ_o is a density parameter which measures the density of the mantle relative to sea water density (Figure 2).

The overall objective of the modeling is to establish a set of parameters which sensitively characterize the flexural

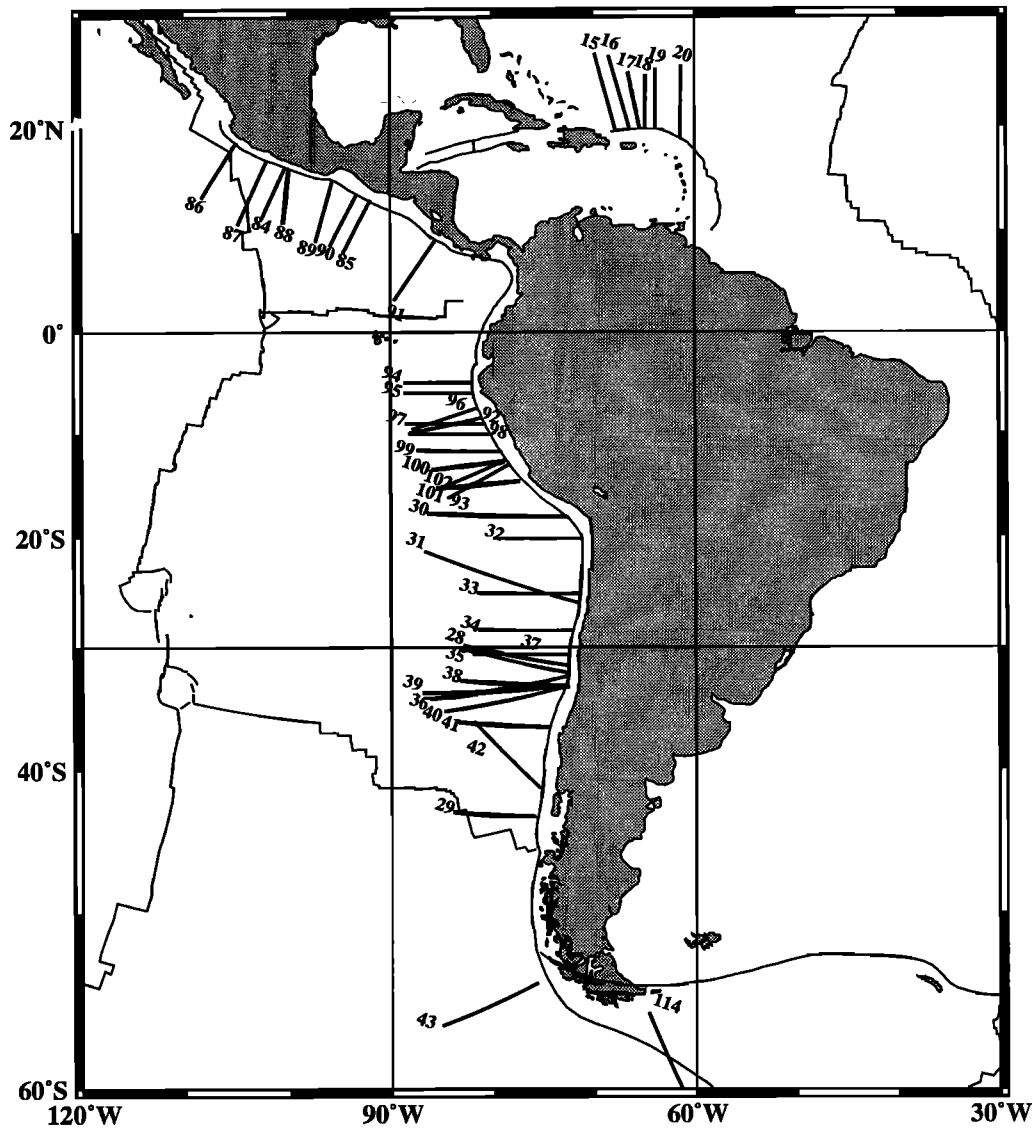


Figure 1c. Global great circle profile location map of Antilles, Chile, Middle America, Peru, and Shetland Trenches. Sandwich profile (113) is not shown for display purposes. End points are presented in Table 1.

behavior of plates experiencing bending at subduction zones. Therefore we wish to find the smallest number of parameters which will simultaneously minimize the misfit between the models (3) and (5) and the topography and gravity data. The most important issue, however, is not the modeling method but the selection, quality and treatment of the data.

Data

Bathymetry

A total of 117 projected great circle bathymetric profiles were obtained for 16 trench-outer rise complexes (Figure 1 and Table 1). Data were acquired from the Lamont-Doherty Earth Observatory on-line geophysical database [Smith, 1993] using GMT software [Wessel and Smith, 1991]. No effort was made to exclude profiles that had poor trench-outer rise signatures unless some obvious feature obscured the trench signature (e.g., aseismic ridges, complete sediment fill, or

indeterminate trench axis location). Later on we use objective criteria to quantitatively eliminate poorly fit profiles. Within a particular complex, projected profile endpoint pairs (trench axis and basin) were selected so that the connecting great circles were in close proximity to long, continuous, straight, nearly trench-normal bathymetric ship tracks. All track data points which fell within a 100-km band of the great circle were retained and projected onto the great circle line. Typical bathymetric profiles are continuous and over 800 km in length, thus constraining mean ocean depth and regional tilt, and are usually less than 20° from normality to trench trend, minimizing cross trend topographic effects. In order to correct data for nonnormality, distance values were multiplied by $\cos\theta$, the angle between the profile and trench-perpendicular azimuths.

Before modeling, gross errors must be corrected in order to reduce deflection perturbation and density bias. Travel time errors occasionally arise due to an ambiguity in analog precision depth recorder (PDR) records [Smith, 1993]. For a

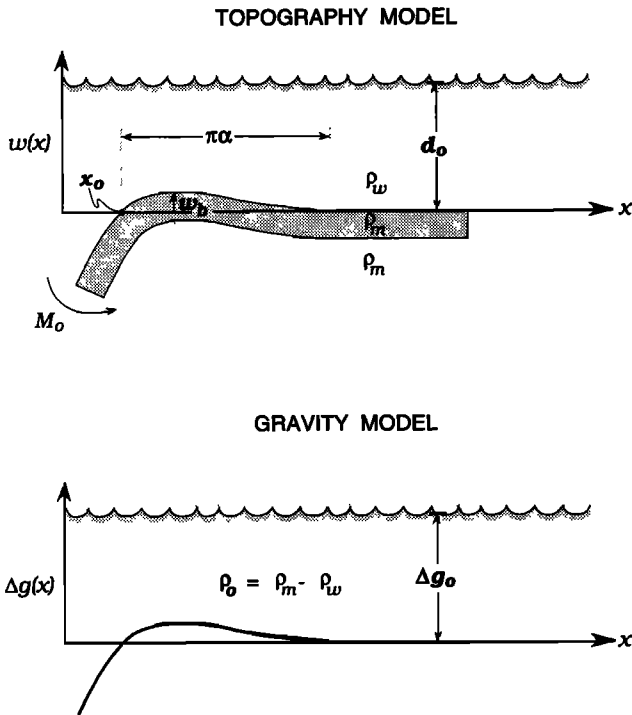


Figure 2. Schematic representation of topography (w_o , x_o , α , and d_o) and gravity (w_o , x_o , α , and g_o) model parameters, where $w_o \sim 3.10 w_b$. See equations (3) and (5) for details of the model. Combined model (topograv) contains all of the above parameters and ρ_o . After application of a depth versus age correction, a regional slope parameter was not required. Topograv parameters are bold.

given trench profile, this error may result in a DC shift of bathymetric depths, appearing as a parallel set of depths above or below the general trend of values. Since these values are clearly erroneous, they were eliminated from each profile before any other processing was performed.

Indiscriminate data acquisition usually results in a nonuniform density of data throughout the profile length (Figure 3, points): crossing tracks result in dense sampling, while course changes and jumps result in data gaps. In order to reduce the biasing effects of erratic densities upon the modeling, a filter was applied to the raw data set. The median value within a 2-km moving window was retained at a 1-km spacing, and importantly, gaps were not filled with dummy values [Wessel and Smith, 1991]. A robust median filter was employed instead of a mean filter so as to minimize the weighting effects of outliers. The filter generally reduced the quantity of data by an order of magnitude while retaining the short-wavelength topographic variations (Figure 3).

The two-way travel time from which depths are determined is a function of the velocity structure of the water column, which is in turn a function of salinity, temperature, and pressure. Smith [1993] reports that these variations in the velocity are ignored and a nominal velocity is arbitrarily assigned to all bathymetric data, resulting in 5% inaccuracies. These nominal depths can be corrected to a first approximation by utilizing tabulated regional depth-related correction factors, or Carter [1980] tables. The filtered profile data were Carter-corrected, having minimal effect for shallow and middepth data, and significant effect with respect to deep-water values.

Thick layers of sediment on the basement topography adversely influence estimates of model parameters in (3). A uniform thickness layer of sediments will reduce the estimate of d_o , while extreme (>400 m) variations in sediment thickness will affect the α estimate, particularly where near the outer trench slope and outer rise. We have not accounted for sediment thickness mainly because sediment thickness data are not available along most of the profiles. Moreover, later we show that where sediment thickness is highly nonuniform, the gravity and bathymetry data will yield inconsistent models that are eliminated from further analysis.

It is known that ocean bottom depth increases with age [Parsons and Sclater, 1977]. Lithospheric ages may vary by tens of millions of years along trench profiles, resulting in age-related depth variation of hundreds of meters, particularly for "young" profiles. In order to minimize this effect, an age-related depth correction was applied to the Carter-corrected profiles. Ages were assigned to every point on a given profile based on a two-dimensional interpolation of an age grid [Roest et al., 1992]. Then each point was corrected for age effects by subtracting the appropriate age formula [Parsons and Sclater, 1977]. For points younger than 20 Ma, we deduct a predicted depth d_{age} :

$$d_{age} = 2500 + 350\sqrt{t} \quad (6)$$

where t is age in Ma. For points older than 20 Ma the correction formula is

$$d_{age} = 6400 - 3200 \exp\left(\frac{-t}{62.8}\right) \quad (7)$$

While this depth-age relationship is known to be variable throughout the ocean basins [Cochran, 1986; Hayes, 1988; Marty and Cazenave, 1989], it is only the first-order depth variations that influence the flexural modeling, since interregional anomalous subsidence will not result in significant differential depth correction within a particular profile. An example of the age correction is shown in Figure 3, top curve; the age correction brings the entire profile to near zero depth.

Local perturbations along profiles due to the presence of seamounts and aseismic ridges were reduced by clipping the topographic highs above a uniform depth. Though such correction often improves the apparent quality of a profile, results obtained from profiles in which topographic noise is substantial must be considered poor.

Gravity

Gravity anomalies were extracted from a global gravity grid [Sandwell and Smith, 1992] which is derived from a combination of ERS 1, Geosat, and Seasat altimeter profiles using the method of Sandwell [1984, 1992]. For areas south of 30°S, where the density of Geosat profiles is relatively high, the satellite-derived gravity anomalies have a precision of 5.5-7 mGal [Sandwell, 1992; Neumann et al., 1993]. In midlatitude areas, where the track density is worse, the anomalies are less accurate, especially at short wavelengths. However, since gravity amplitudes at trenches usually exceed 100 mGal and generally have wavelengths greater than the satellite track spacing (< 60 km), we believe that they are sufficiently accurate.

Table 1. Profile End Points, Model Ages, and Parameters

Trench	Start		End		Age*, Ma	Misfit, m	w_o , m	d_o , m	α , km	Range ⁺ , km	ρ_o , kg m ⁻³	K_o , 10 ⁻⁷ m ⁻¹	M_o , 10 ¹⁶ N	h_e , km	h_m , km
	Latitude	Longitude	Latitude	Longitude											
1	50.4	180.1	44.1	180.2	58.0	0.312	1712.7	-328.8	63.2	21.0	2048	8.58	7.38	24.6	36.6
2	50.3	181.0	44.0	181.0	58.0	0.312	1767.8	-291.0	67.1	24.0	2200	7.85	8.6	26.7	38.5
3	50.5	185.4	43.6	185.4	57.6	0.462	1496.8	-383.8	82.2	67.0	2200	-	-	-	-
4	50.9	188.6	45.7	190.1	58.3	0.405	613.4	-11.3	47.2	55.0	2300	-	-	-	-
5	50.3	182.1	44.0	179.5	57.9	0.309	2082.2	-315.1	62.6	19.0	2200	10.6	8.81	24.3	38.2
6	52.3	193.6	47.8	198.8	59.4	0.224	540.5	280.6	62.6	58.0	2383	-	-	-	-
7	52.7	195.8	47.9	200.2	58.1	0.298	880.8	228.4	83.9	54.0	2096	2.50	6.69	35.9	41.2
8	50.5	183.4	44.5	182.8	58.0	0.337	1779.0	-264.5	68.3	28.0	2206	7.63	8.95	27.3	39.8
9	52.7	195.1	45.0	195.2	58.6	0.252	794.8	175.4	84.2	35.0	2199	2.24	6.08	36.1	40
10	57.2	211.6	52.4	222.3	43.8	0.432	932.7	577.4	110.6	70.0	2200	1.52	12.3	51.9	61
11	53.9	202.0	45.6	202.0	56.4	0.476	662.7	259.6	89.5	125.0	2199	-	-	-	-
12	54.0	202.8	48.4	215.1	55.4	0.301	1490.3	140.4	102.9	35.0	1598	-	-	-	-
13	55.8	209.7	52.5	223.7	42.8	0.526	62.0	520.2	31.7	53.0	1882	-	-	-	-
14	51.4	190.8	41.8	191.0	60.0	0.624	638.8	-120.9	49.6	82.0	2819	-	-	-	-
15	19.7	292.2	26.8	290.1	109.3	0.736	386.0	458.3	21.4	64.0	700	-	-	-	-
16	19.8	293.6	26.6	291.5	111.0	0.327	1424.7	144.4	73.9	43.0	2200	5.21	8.41	30.3	40.5
17	19.9	294.6	25.1	293.4	103.3	0.209	1315.2	-9.1	68.7	18.0	2200	5.58	6.69	27.5	36.4
18	19.8	295.1	24.9	295.2	101.2	0.161	1819.5	-100.2	69.3	11.0	2076	7.57	9.44	27.8	40.3
19	19.9	296.1	25.4	296.1	97.5	0.305	1851.8	-133.6	77.7	16.0	2050	6.14	12.1	32.4	45.2
20	18.9	298.6	25.7	298.7	87.3	0.424	1587.6	-290.2	74.5	44.0	2200	5.72	9.51	30.6	41.3
21	29.7	142.7	30.8	150.4	141.8	0.265	1836.8	-104.3	65.8	23.0	1797	8.48	8.59	26	38.8
22	28.8	143.0	30.0	150.6	142.2	0.290	1534.0	-129.1	85.2	51.0	1795	4.23	12	36.6	47
23	27.9	143.3	29.1	151.7	143.2	0.339	954.2	38.9	84.3	73.0	1467	-	-	-	-
24	31.1	142.3	32.3	151.7	141.7	0.414	336.9	108.5	35.0	75.0	2074	-	-	-	-
25	32.5	142.1	33.6	151.7	140.7	0.363	1791.6	79.6	114.2	77.0	2245	2.75	25.2	54.1	75
26	33.5	142.0	34.6	151.7	140.9	0.361	1706.1	161.0	80.9	46.0	1860	5.21	12.1	34.2	46.7
27	34.5	142.0	35.6	151.7	139.9	0.340	601.0	231.1	46.2	66.0	2366	-	-	-	-
28	-31.6	287.4	-29.8	277.1	40.0	0.476	1079.3	423.5	57.6	37.0	2322	6.5	3.86	21.7	28.4
29	-43.5	284.1	-43.1	276.0	13.6	0.564	1239.9	-100.4	82.1	44.0	269	-	-	-	-
30	-18.1	287.1	-17.7	273.6	41.9	0.530	1239.2	59.0	71.2	70.0	2101	-	-	-	-
31	-26.1	288.5	-21.3	273.3	43.9	0.599	2442.7	305.8	150.6	187.0	1189	-	-	-	-
32	-20.1	288.7	-20.1	280.9	49.3	0.460	2971.1	-113.9	74.6	37.0	1027	-	-	-	-
33	-25.2	288.5	-25.1	278.5	44.2	0.610	1220.9	510.6	148.0	222.0	2200	-	-	-	-
34	-28.5	287.9	-28.4	278.6	41.8	0.365	537.2	516.3	62.1	63.0	1740	-	-	-	-
35	-32.2	287.3	-30.1	277.1	39.5	0.448	528.3	550.1	35.9	46.0	2604	-	-	-	-
36	-32.5	287.2	-34.4	273.8	38.9	0.318	2178.1	359.1	64.6	17.0	1471	-	-	-	-
37	-30.6	287.5	-30.5	278.0	40.4	0.455	632.8	396.6	56.2	44.0	2254	-	-	-	-
38	-33.3	287.2	-32.8	276.8	36.7	0.429	1483.8	421.8	58.2	29.0	2442	8.75	5.43	22.1	32.4
39	-33.2	287.3	-33.9	273.1	36.7	0.493	1466.8	423.3	60.6	35.0	2237	7.99	5.81	23.3	33.5
40	-33.3	287.4	-35.4	275.2	36.4	0.481	718.5	462.8	78.0	51.0	3516	-	-	-	-
41	-36.7	285.4	-36.2	276.6	32.2	0.434	327.7	351.5	66.6	53.0	3099	-	-	-	-
42	-41.4	284.6	-36.2	278.1	21.0	0.913	-22.1	288.5	48.3	161.0	2199	-	-	-	-
43	-54.3	284.3	-56.7	274.9	20.2	0.624	1021.7	-149.2	123.4	72.0	1615	-	-	-	-
44	-58.1	157.6	-58.0	149.6	15.6	0.327	591.9	458.5	39.3	36.0	2087	-	-	-	-

Table 1. (continued)

Trench	Start		End		Age*, Ma	Misfit, m	w _o , m	d _o , m	α, km	Range [†] , km	ρ _o , kg m ⁻³	K _o , 10 ⁻⁷ m ⁻¹	M _o , 10 ¹⁶ N	h _e , km	h _m , km
	Latitude	Longitude	Latitude	Longitude											
45 japan1	39.3	144.3	38.0	153.7	132.0	0.312	1625.2	266.4	117.1	48.0	2028	2.37	24.1	56	72
46 japan2	41.7	145.7	37.7	155.2	127.0	0.416	602.3	510.0	86.8	65.0	3675	-	-	-	-
47 japan3	40.6	144.5	38.0	154.4	130.0	0.376	1475.2	387.5	125.9	55.0	2241	1.86	25.2	61.7	70
48 japan4	37.0	143.4	37.0	154.2	135.1	0.321	994.1	189.2	119.3	66.0	2381	1.4	15.3	57.4	63
49 japan5	36.1	142.9	36.0	153.6	135.9	0.553	237.8	263.0	46.7	122.0	2607	-	-	-	-
50 japan6	34.9	142.1	35.3	152.1	139.3	0.388	897.5	176.8	60.2	51.0	2240	-	-	-	-
51 japan7	34.0	141.9	34.0	151.3	140.6	0.325	1562.3	172.3	53.3	40.0	1750	-	-	-	-
52 japan8	34.6	142.0	33.4	151.3	140.0	0.416	1986.6	101.8	94.9	71.0	2200	-	-	-	-
53 japan9	32.4	142.1	32.2	151.7	140.8	0.317	1100.5	142.4	71.7	57.0	2199	-	-	-	-
54 japan10	34.7	142.0	32.3	150.8	140.1	0.438	929.0	237.0	56.1	70.0	2199	-	-	-	-
55 java3	-6.9	102.2	-8.4	97.8	71.8	0.520	591.9	-111.7	43.3	29.0	1673	-	-	-	-
56 java4	-9.5	106.0	-14.1	106.2	82.1	0.388	2639.2	-101.6	57.1	20.0	1679	-	-	-	-
57 java5	-10.1	108.7	-19.1	107.5	85.8	0.768	209.1	300.0	21.7	215.0	2016	-	-	-	-
58 java6	-3.0	99.0	-7.6	94.0	58.9	0.467	2089.1	-76.1	112.4	65.0	1227	-	-	-	-
59 java7	-11.3	115.8	-15.6	115.5	92.3	0.365	1381.3	-59.4	84.1	40.0	2199	3.9	10.5	36	45
60 java11	-11.3	117.8	-15.7	117.9	93.9	0.252	836.2	-55.0	61.8	16.0	2196	4.38	3.44	23.9	29.2
61 java13	0.1	96.8	-4.1	93.1	47.9	0.626	511.6	136.7	74.3	106.0	2070	-	-	-	-
62 kermadec1	-33.6	182.4	-36.1	195.0	95.5	0.651	258.7	34.6	49.4	230.0	1800	-	-	-	-
63 kermadec2	-35.2	181.3	-34.4	195.0	94.8	0.335	262.9	52.5	60.9	72.0	2200	-	-	-	-
64 kermadec4	-30.3	183.3	-29.8	194.2	96.9	0.582	354.1	176.8	26.9	161.0	2355	-	-	-	-
65 kuril2	47.5	155.7	41.3	162.9	114.8	0.473	2006.3	554.5	106.7	80.0	2199	-	-	-	-
66 kuril3	47.4	155.2	38.9	159.1	116.1	0.365	1963.6	467.8	109.4	37.0	2200	3.28	25.4	51.2	71
67 kuril4	45.3	152.9	38.7	159.1	120.3	0.265	1325.1	451.7	66.2	22.0	2359	6.05	6.27	26.2	35
68 kuril5	42.6	148.1	38.3	156.7	120.0	0.363	1729.9	359.2	120.2	66.0	2200	2.39	27	58	75
69 kuril6	44.3	150.9	36.4	154.4	122.6	0.229	2589.5	316.8	103.9	26.0	1748	4.8	30.2	47.7	70
70 kuril7	42.1	146.9	35.6	153.2	120.0	0.446	1023.3	428.9	70.5	94.0	2491	-	-	-	-
71 kuril8	42.0	146.4	37.8	156.7	120.0	0.372	1175.3	366.6	110.1	89.0	2586	-	-	-	-
72 kuril9	51.3	160.4	44.8	166.1	100.2	0.523	1267.4	-10.7	128.1	110.0	1848	-	-	-	-
73 kuril10	46.1	154.0	42.2	162.9	118.1	0.286	2056.8	495.2	94.8	31.0	2029	4.57	20	42.3	57.8
74 mariana1	23.8	143.8	26.3	153.1	145.4	0.592	1887.2	289.6	72.4	46.0	2200	-	-	-	-
75 mariana2	23.2	144.8	25.7	154.9	146.1	0.575	173.9	272.4	47.8	76.0	2733	-	-	-	-
76 mariana3	22.4	145.7	25.2	157.6	148.1	0.600	463.5	376.2	78.4	126.0	2200	-	-	-	-
77 mariana4	21.7	146.6	24.0	157.3	148.7	0.588	171.0	454.1	29.2	89.0	2520	-	-	-	-
78 mariana7	14.9	147.6	15.5	158.3	152.5	0.857	636.0	168.3	132.7	236.0	2199	-	-	-	-
79 mariana8	12.9	146.1	10.7	155.4	144.0	0.307	2523.0	183.9	88.6	28.0	1947	6.43	21.4	38.6	57
80 mariana9	12.6	145.9	10.4	151.1	142.7	0.308	1339.7	237.0	67.8	32.0	1928	5.83	6.65	27	36.4
81 mariana10	12.1	145.2	6.2	154.8	140.6	0.588	650.4	950.2	58.2	79.0	1307	-	-	-	-
82 mariana11	11.0	141.7	2.9	151.9	133.3	0.684	7350.3	150.0	618.0	409.0	894	-	-	-	-
83 mariana12	10.9	140.0	2.7	140.0	130.3	0.847	5194.7	1692.8	242.1	22.0	436	-	-	-	-
84 middle1	16.3	259.8	11.3	257.5	11.1	0.510	638.5	-10.9	44.9	52.0	1797	-	-	-	-
85 middle2	13.1	268.1	7.9	265.4	27.3	0.327	1241.1	179.1	71.8	33.0	1881	4.82	6.90	29.1	37.5
86 middle3	18.7	255.1	13.3	251.7	1.7	0.666	461.6	-357.7	48.8	122.0	1377	-	-	-	-
87 middle4	16.9	258.0	10.7	255.2	7.5	0.587	505.6	-204.8	51.2	54.0	2178	-	-	-	-
88 middle5	16.1	260.2	10.8	259.5	12.6	0.345	415.4	156.0	43.5	30.0	2231	4.39	0.848	15	17.2
89 middle7	15.1	264.4	9.0	262.7	22.6	0.710	626.5	-58.3	43.6	92.0	2200	-	-	-	-
90 middle8	13.7	266.8	8.6	264.1	24.8	0.569	833.4	-13.4	64.4	66.0	2483	-	-	-	-
91 middle9	9.2	274.5	3.2	270.4	27.3	0.741	2331.2	723.9	75.4	76.0	587	-	-	-	-

Table 1. (continued)

	Trench	Start		End		Age*, Ma	Misfit, m	w_0 , m	d_0 , m	α , km	Range [†] , km	ρ_0 , kg m ⁻³	K_0 , 10 ⁻⁷ m ⁻¹	M_0 , 10 ¹⁶ N	h_e , km	h_m , km
		Latitude	Longitude	Latitude	Longitude											
92	peru1	-8.5	278.9	-10.0	271.8	29.5	0.352	213.6	-73.8	59.2	84.0	2018	-	-	-	-
93	peru2	-13.0	281.7	-16.3	275.6	38.9	0.552	314.8	-88.6	90.6	152.0	4741	-	-	-	-
94	peru3	-5.0	278.1	-5.0	271.3	29.7	0.520	443.2	470.2	75.5	79.0	1986	-	-	-	-
95	peru4	-6.1	278.2	-6.0	271.3	29.4	0.409	379.5	285.0	58.8	64.0	1931	-	-	-	-
96	peru5	-7.5	278.6	-9.6	272.1	29.5	0.342	598.1	-75.9	90.4	55.0	2199	1.46	5.28	39.7	46
97	peru6	-9.1	279.2	-9.0	271.4	29.5	0.354	205.4	-93.8	60.8	88.0	2200	-	-	-	-
98	peru7	-10.1	279.7	-10.0	271.9	29.5	0.383	228.0	-199.4	81.0	78.0	2159	-	-	-	-
99	peru8	-11.8	280.7	-11.6	272.6	36.2	0.454	488.2	-163.6	69.9	44.0	1837	2	2.58	28.2	30.2
100	peru9	-12.6	281.4	-13.6	274.0	38.7	0.602	160.1	-89.4	48.8	190.0	2741	-	-	-	-
101	peru10	-12.6	281.4	-15.3	275.0	38.8	0.323	1060.1	-233.5	108.1	52.0	2061	1.81	13.4	50.4	58
102	peru11	-14.6	282.7	-15.4	274.5	39.4	0.359	2154.1	-222.8	126.6	45.0	902	-	-	-	-
103	philippine3	13.4	125.6	13.4	133.0	117.6	0.536	2835.7	23.2	118.7	69.0	484	-	-	-	-
104	philippine4	13.5	125.5	15.0	131.7	117.9	0.477	1029.7	387.7	117.1	64.0	1701	1.5	15.2	56	62
105	philippine5	10.8	126.6	11.4	134.0	116.2	0.467	314.2	198.4	45.1	135.0	2200	-	-	-	-
106	philippine6	10.8	126.5	12.7	133.6	116.4	0.470	555.8	124.8	24.6	150.0	1713	-	-	-	-
107	philippine7	9.2	126.9	10.5	134.1	115.3	0.668	331.6	61.9	42.1	141.0	2200	-	-	-	-
108	philippine8	7.4	127.2	12.9	133.9	113.9	0.737	2856.4	9.6	52.8	108.0	1254	-	-	-	-
109	philippine9	6.0	127.5	7.3	131.0	112.5	0.396	1067.1	323.6	53.3	71.0	2118	-	-	-	-
110	philippine10	4.3	128.3	4.0	141.2	111.3	0.641	3536.2	571.5	355.6	387.0	836	-	-	-	-
111	philippine11	4.9	128.0	7.5	131.9	111.7	0.306	1616.8	315.2	47.7	22.0	1503	-	-	-	-
112	philippine12	4.1	128.6	9.7	138.9	111.3	0.722	806.1	638.0	95.0	200.0	2207	-	-	-	-
113	sandwich1	-55.8	334.8	-51.6	351.0	72.8	0.449	3239.7	523.4	89.2	52.0	962	-	-	-	-
114	shetland1	-61.3	299.8	-56.0	295.2	16.3	0.869	528.9	1731.6	251.4	16.0	2200	-	-	-	-
115	tonga1	-24.6	184.8	-27.2	195.0	100.1	0.477	996.3	101.6	69.3	110.0	1869	-	-	-	-
116	tonga2	-21.9	186.1	-23.7	194.2	101.4	0.366	319.2	-19.2	81.1	70.0	2836	-	-	-	-
117	tonga3	-22.4	186.0	-22.2	193.2	101.3	0.374	254.2	-3.3	71.8	61.0	2326	-	-	-	-

Fractional misfit, flexural amplitude, regional depth, flexural parameter, 10% flexural parameter range, and lithospheric density obtained using the topograv modeling scheme. Curvature, bending moment, and effective elastic thickness are determined by the thin elastic plate model, with mechanical thickness values determined using the h_e to h_m conversion method proposed by *McNutt and Menard* [1982], for "successfully" fit topograv ($\lambda = 0.4$). Data for grav ($\lambda = \infty$) and topo ($\lambda = 0$) are available on microfiche.

* Age [Roest *et al.*, 1992] is measured at first zero crossing seaward of trench axis.

† Range is the difference between the maximum and minimum α . Note that the range is not always centered at α .

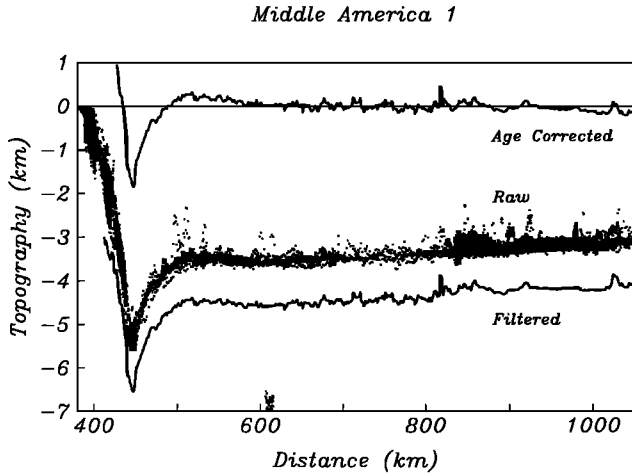


Figure 3. Raw, filtered, and age-corrected plots of the Middle America 1 profile data (84). One-kilometer window, median filter data are shifted 1 km downward from raw data for presentation. Age-corrected data are displayed with reference to zero depth.

Flexural Modeling

Age-corrected topographic profile data and gravity were modeled by fitting them to the topographic model (3) and gravity model (5), respectively. We develop a misfit formula which minimizes the difference between observed data and predicted values in order to obtain a best fitting parameter set for six model parameters: w_o , ρ_o , α , x_o , d_o , and Δg_o . (Below we discuss the rationale for not using a slope parameter in the topographic model.) Note that this is a nonlinear parameter estimation problem in both x_o and α so a standard linear least squares approach cannot be used and there may be local minima that do not correspond to the global minimum. The minimization algorithm we use is the downhill simplex method [Nelder and Mead, 1965], implemented in Matlab [Mathworks, 1993]. This is a multidimensional minimization that requires only function evaluations without derivatives. The downhill simplex method is started with an initial multidimensional point, defining the initial simplex. The method then takes a series of steps (reflections, expansions and contractions within parameter space) until a tolerance limit is reached in the change of the function value or the change in the magnitude of the parameter vector. The algorithm locates the first local minimum which satisfies the tolerance criteria. Therefore it is critical to determine the sensitivity of minimum misfit estimates to the initial parameter set. If the minimum obtained by the simplex minimization scheme varies substantially for reasonable starting guesses, then the method may be considered inappropriate, as the method and not the data is constraining the best fit model parameters.

The downhill simplex method can accommodate almost any reasonable type of minimization so we have devised a function to simultaneously optimize topography and gravity fits. First, in order to reduce sensitivity to seamounts and other large topographic features, the sum of the absolute residuals (data - model), rather than rms misfit is calculated. Second, since we wish to model outer rise profiles with distant, seaward portions of profiles serving only to constrain the undeflected profile depth, the data were assigned a weight that decreases

linearly with distance from the trench axis. Third, the residuals are normalized by the absolute deviation of the data from the mean (the "linear" variance). The total misfit is

$$\psi = \frac{1}{(1 + \lambda)} \left[\sum_{i=1}^N \frac{|w_i - w(x_i)|}{\sigma_w} + \lambda \sum_{i=1}^N \frac{|\Delta g_i - \Delta g(x_i)|}{\sigma_{\Delta g}} \right], \quad (8)$$

where the linear variances of the deflection σ_w and gravity $\sigma_{\Delta g}$ are given by

$$\sigma_w = \sum_{i=1}^N |w_i - d_d| \quad \sigma_{\Delta g} = \sum_{i=1}^N |\Delta g_i - \Delta g_d|. \quad (9)$$

N is the number of data points, $w(x_i)$ and $\Delta g(x_i)$ are the model topography and gravity, w_i and Δg_i are the observed topography and gravity, and λ is a parameter that scales the weight of the topography relative to the weight of the gravity data; later we will set λ to 0 (topo), 0.4 (topograv), and ∞ (grav). The L_1 norm misfit parameter ψ is a measure of the improvement of the six-parameter model over a two-parameter model, d_o and Δg_o .

Prior to the complete analysis, we tested whether or not a regional topographic slope is needed to obtain reliable fits to the topographic profiles. McQueen and Lambeck [1989] have suggested that regional topographic tilt, due to poor depth/age correction, thermal swell, or dynamic uplift, has a significant effect on elastic fit models, which, if left unaccounted for, results in poor and biased estimates of model parameters. We used a least squares minimization on the topography data so that established statistical tests could be utilized (e.g., F test). In the majority of cases, the models displayed good visual fits to the data, regardless of presence or absence of free tilt. We believe the lack of significant tilt in most of our profiles is due to the improved age model provided by Roest *et al.* [1992]. In most cases where both models converge on similar outer rise dimensions, the fractional misfit yielded by the free-tilt model is marginally lower than that obtained by a fixed-tilt model. However, sensitivity to the relevant parameters is sacrificed. Figure 4a shows a typical profile obtained at the Aleutian Trench, containing a medium-sized outer rise, nearly no regional tilt, and relatively noise-free topography. The fixed- and free-tilt models appear to fit the topography equally well (Figure 4a) and result in similar flexural parameters (no tilt, 59.5 km; tilt, 62.2 km) and similar flexural amplitudes (no tilt, 1.53 km; tilt, 1.72 km). The modest positive tilt accommodates a gentle slope seaward of the trench and outer rise. Plots of fractional rms misfit as a function of α for the best fit model (Figure 4b) demonstrate that there is a slight decrease in misfit for the free tilt model (< 1%). However, the increase in the width about the minimum of the misfit curve (dashed) confirms the loss in sensitivity of the free-tilt model to the flexural wavelength [McQueen and Lambeck, 1989]. Furthermore, the mutual dependence of the model parameters implies that the tilt term is altering the wavelength value.

In contrast to this Aleutian Trench profile which has low tilt, we also selected a profile at the Middle America Trench which displays moderate tilt (Figure 4c). In this case, the free-tilt model provides an improved fit to the data (Figure 4d) and results in a shorter flexural parameter (no tilt, 56 km; tilt, 30 km) and a lower flexural amplitude (no tilt, 0.85 km; tilt, 0.26 km). Because the tilt is large relative to the amplitude of the flexure, the fixed-tilt model probably provides a poor estimate of the flexural parameter. Conversely, while the free-tilt model provides a better fit to the data (improved misfit by >10%) it

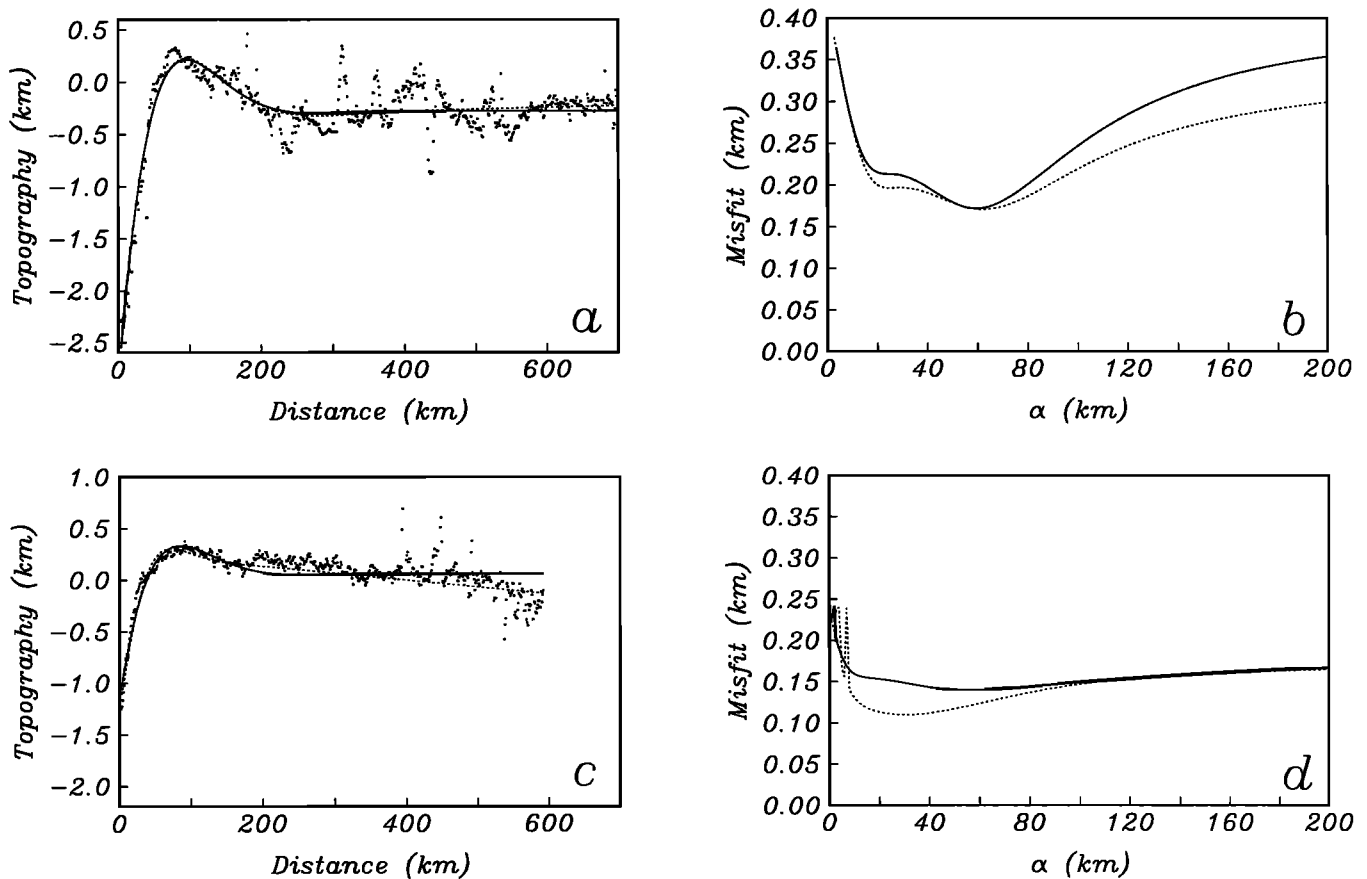


Figure 4. (a) Best fit RMS models for the Aleutian 1 profile (1). Solid line corresponds to a zero, fixed-slope model. Dashed line corresponds to a free-slope model. (b) Best fit RMS misfit values for a range of flexural parameter values (α) for the Aleutian 1 profile (1). Solid line corresponds to a zero, fixed slope model. Dashed line corresponds to a free slope model. (c) Same as Figure 4a for the Middle America 5 profile (88). (d) Same as Figure 4b for the Middle America 5 profile (88).

probably estimates slopes well and the flexural parameters poorly.

In general, a tangible improvement in model misfit is necessary in order to justify the substantial decrease in sensitivity to the parameters of interest. An F test comparing the variances of both models fails to justify the use of the additional tilt parameter at the 90% confidence level even for the most tilted profiles. Considering the loss in sensitivity to the parameters of interest and minimal improvement in misfit we chose not to include the tilt parameter. In addition, the gravity anomaly profiles provide the additional information needed to reduce the error caused by our fixed-tilt assumption.

Results

The bathymetry and gravity data were fit to formula (8) with λ values of 0, ∞ , and 0.4, which correspond to fitting topography (topo), gravity (grav), and combined topography-gravity (topograv) with a respective topography-gravity weight ratio of 2.5 / 1, which reflects our emphasis on original depth soundings over gridded altimeter gravity. The bathymetry data set is characterized by higher precision and superior short-wavelength resolution to the gridded and interpolated gravity even south of 30°S, where unclassified altimetry allows for increased resolution. The topographic

modeling is limited to the parameters, w_o , x_o , d_o , and α , the gravity modeling is limited to the parameters w_o , x_o , Δg_o , and α , and the combined modeling contains the parameters w_o , x_o , d_o , Δg_o , α , and ρ_o . Table 1 lists the best fit modeling parameters (w_o , d_o , α , and ρ_o only) and misfit values for topograv with misfits and 10% alpha ranges (for alpha range discussion, see below; complete data for the three fitting schemes are available on microfiche¹). The simplex minimization algorithm generally required several hundred iterations for reasonable starting values. Restarts with varied, though similar, initial values yielded consistent results with a nominal precision, set by the tolerance limits, of the parameter value. One hundred and nine of the original profiles were successfully fit to some extent by at least one of the procedures. Figure 5 shows the model fitting to the topography and gravity of all of the profiles used in the study.

Though the models provide fits to all of the profiles, the utilization of the parameterization for flexural analysis requires a mechanism by which bad or suspect data can be eliminated. Visual inspection only provides a qualitative,

¹Supplementary data are available with entire article on microfiche. Order from American Geophysical Union, 2000 Florida Avenue, N.W., Washington, DC 20009. Document B94-004; \$2.50. Payment must accompany order.

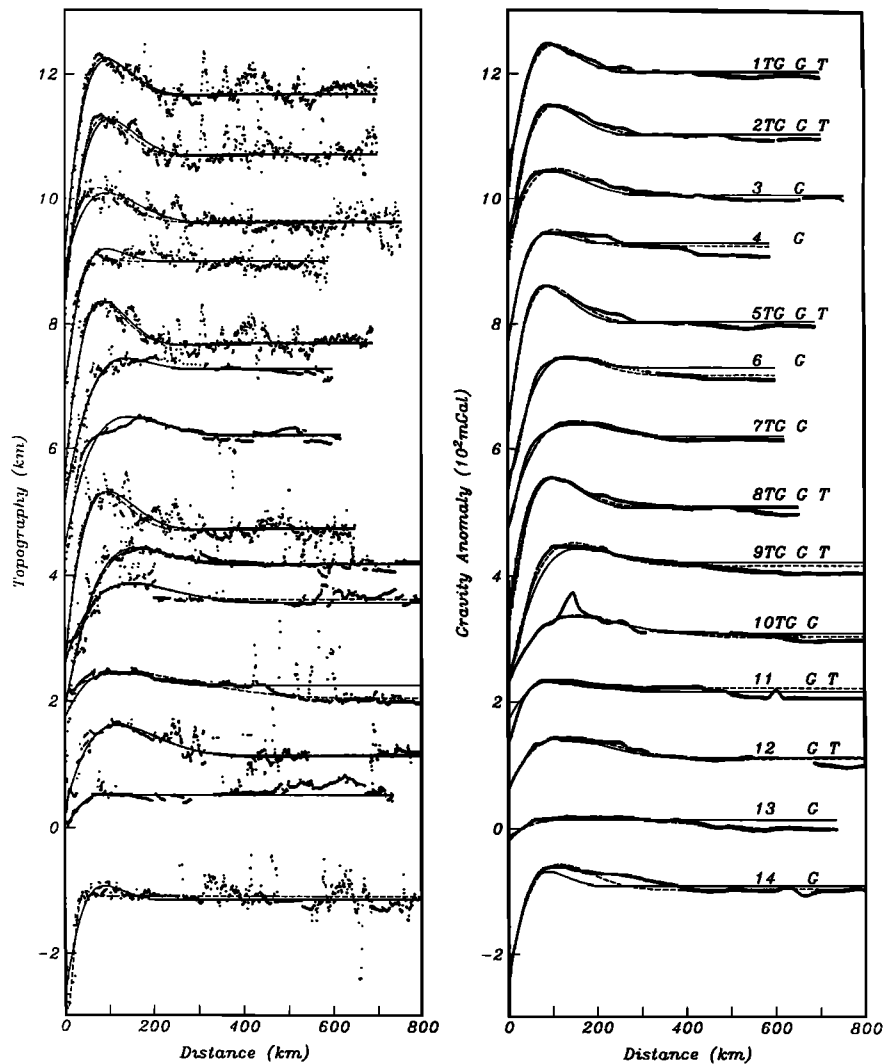


Figure 5. Topography and gravity data for 117 profiles modeled in the study. Profiles are arbitrarily shifted vertically for presentation. For topography (shown at left), solid lines correspond to the best fit model for topograv ($\lambda = 0.4$) and dashed lines correspond to the best fit model for topo ($\lambda = 0$). For gravity (shown at right), solid lines correspond to the best fit model for topograv ($\lambda = 0.4$) and dashed lines correspond to the best fit model for grav ($\lambda = \infty$). Profiles are numbered according to the numbering scheme of Table 1. TG, G, and T mark profiles that were "successfully" modeled by topograv, grav, and topo, respectively.

approximate discrimination regarding adequacy of fit and precision of parameter estimation. In an effort to quantitatively evaluate fit, three semiobjective criteria were established that, in general, coincided with our intuitive expectations:

1. Acceptable profiles must have a misfit of less than 0.5, which means that the addition of the flexure parameters reduces the variance by 50% with respect to the model with just a mean depth (and/or gravity) as a parameter.

2. In an effort to determine the sensitivity of the model to the flexural parameter (α), the fitting procedure was performed for each profile by varying a fixed alpha value until a 10% increase in misfit had resulted, establishing conservative "error bars" for flexural wavelength. The 10% alpha range must not exceed 0.7 of the alpha value.

3. For topograv fits only, profiles were kept when the modeled density contrast ρ_o was within the range 1700-2600 kg m^{-3} . When both gravity and topography were modeled, the

density contrast parameter was usually about 2200 kg m^{-3} corresponding to an uncompensated outer rise with a mantle density of 3200 kg m^{-3} . Lower densities indicate that the outer rise consists of partially compensated topography (i.e., profile 102, Figure 5, $\rho_o = 902 \text{ kg m}^{-3}$), while higher densities may reflect areas of thick sediment cover that reduces the topographic signal but preserves most of the gravity signal. A primary asset of the topograv approach is the ability, unlike in previous studies, to discriminate between fits to flexural and nonflexural topography.

In this manner, 37 topograv, 47 topo, and 108 grav profiles were considered acceptable for further analysis of flexural behavior (Figure 5). The validity of the flexural modeling technique for the inversion of systematic variations of elastic thickness, flexural rigidity, applied moment, and other bending parameters is greatly limited by the presence of short- and long-wavelength bathymetric noise. By averaging nearby profiles, we have greatly diminished the weight of

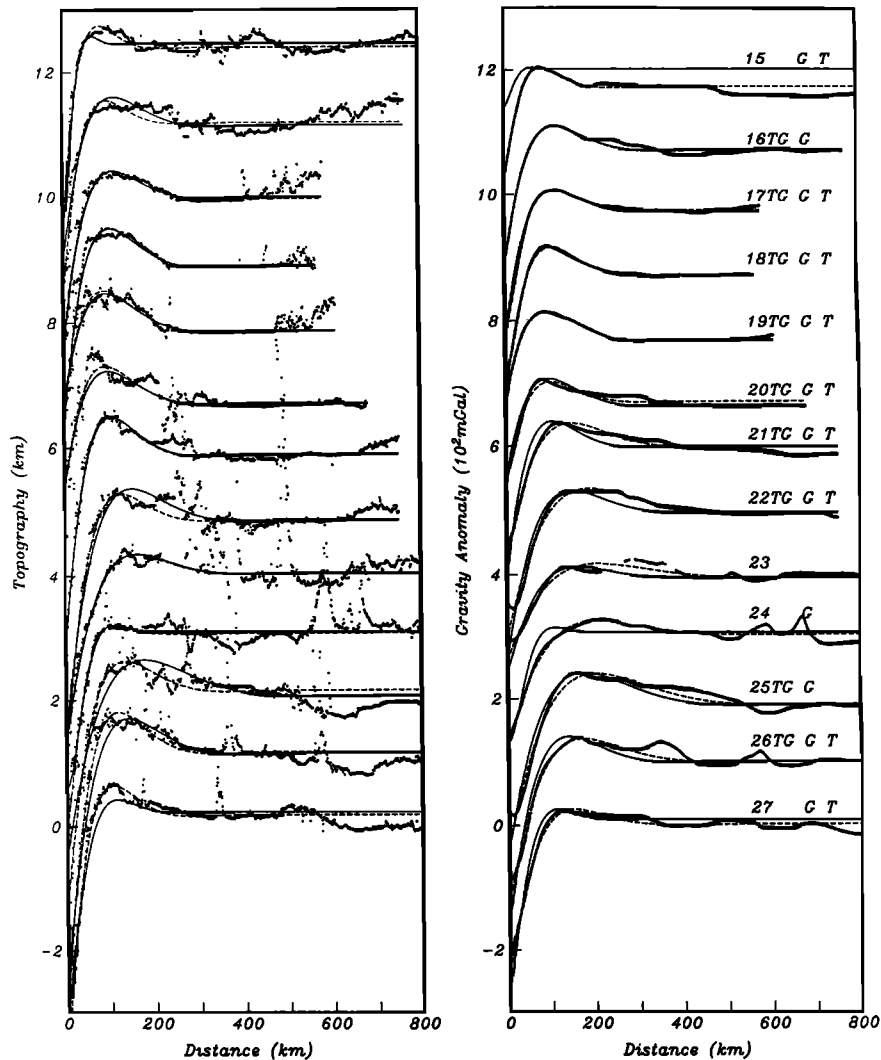


Figure 5. (continued)

uncorrelated, short-wavelength features. Nevertheless, the bathymetry retains a sensitivity to nonflexural long-wavelength, bathymetric features (non-age-related regional tilt and swell, irregular sediment deposition, outer rise shaped nonflexural topography), which limit the accuracy of parameters inferred based on fitting topography alone. Satellite altimeter gravity modeling reflects the effect of deeper structures [McQueen and Lambeck, 1989] and is less dependent on surface deformational effects.

Figure 6 shows the flexural parameter values obtained from the topograv modeling procedure against the grid-derived age at the first zero crossing, along with the 10% alpha ranges for each of the topograv data points. To a limited extent, the fact that the three flexural parameter estimates coincide, falling consistently within the topograv 10% range, confirms a correlation between the two data sets and establishes the 10% range as conservative with respect to the true wavelength value. The flexural parameter α displays a positive age correlation (Figure 6), particularly with respect to the gravity parameter set. However, the α obtained by the gravity modeling usually exceeds the α obtained from the topographic modeling. This behavior has been noted by McAdoo and Martin [1984] and by Judge and McNutt [1991] and has been

attributed to attenuation of short-wavelength noise (i.e., seamounts) by the gravity representation.

The topograv modeling approach allows for the rejection of profiles for which the topography and gravity modeling schemes yield divergent parameter values. Eighteen profiles that were adequately fit by the topography and gravity modeling separately were not fit by the combined model. Where topo and grav flexural parameter values were substantially different (see profiles 11, 50, and 111), the fit to the combined data set was moderately poor and the 10% alpha range was large, reflecting a compromised fit over a wide range of flexural parameter values. The wavelength sensitivity criterion effectively removed the vast majority of profiles for which the flexural parameter values differed by more than 15 km (mean $\alpha_{\text{grav}} / \alpha_{\text{topo}} = 0.88$, s.d. = 0.19, for quality topograv fits). In our modeling scheme, the estimated α is usually closer to either the topo or grav estimates rather than lying between the two. Moreover, the model generally favors a fit to the topographic wavelength because the topography data are more heavily weighted (mean $\alpha_{\text{topograv}} / \alpha_{\text{topo}} = 1.07$, s.d. = 0.13, for quality topograv fits). Even where separate topographic and gravity modeling yielded similar flexural parameter values, profiles were rejected where the

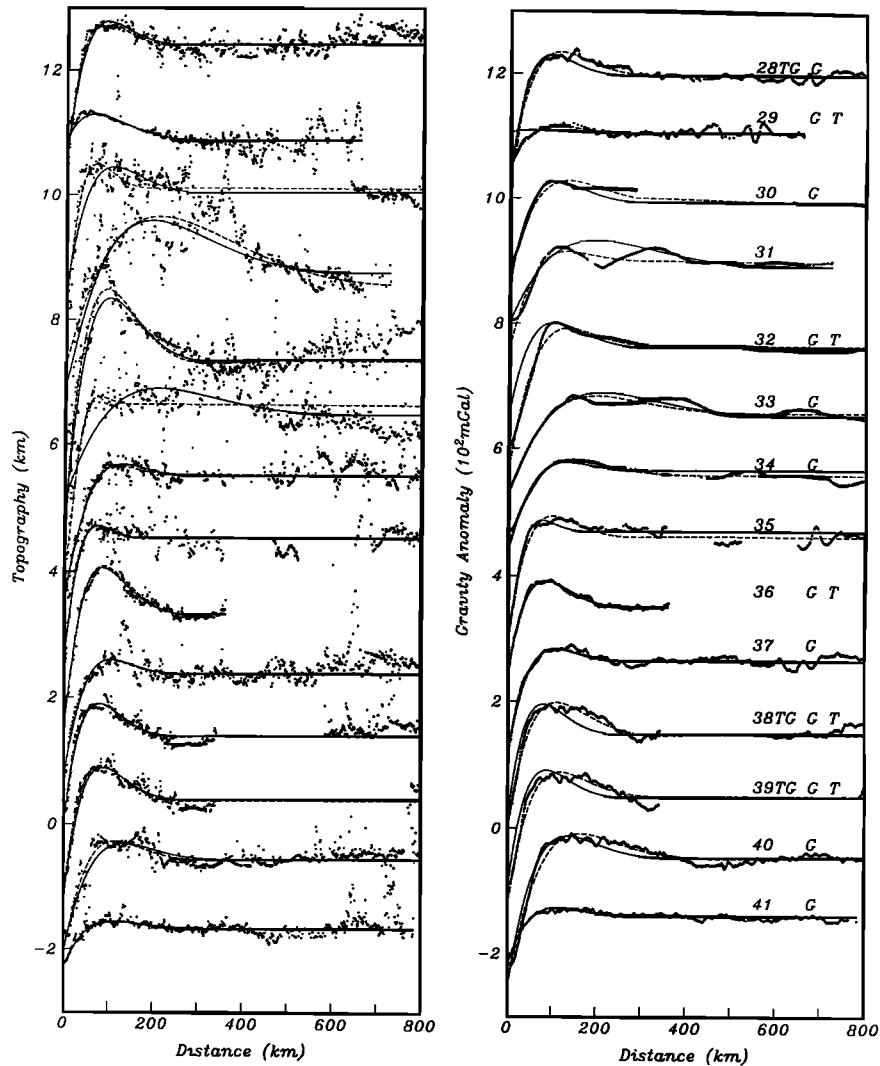


Figure 5. (continued)

mantle-water density contrast parameter was outside the acceptable range (usually below 1700 kg m^{-3} ; for example, profiles 36 and 58). In these cases, the flexural amplitude parameter (and the bending moment value, below) is highly suspect because the model may be fitting nonflexural topography.

Profiles which could not be adequately fit by modeling topography alone were successfully fit in the combined modeling scheme. Where the topo misfit value was marginally unacceptable, a well-fit gravity model with a similar α value to the topo model and a reasonable ρ_0 value, could diminish the total misfit in the combined topograv model (see profiles 99 and 104). Where a small outer rise and/or a substantial bathymetric noise component allowed for an inadmissible wide-ranging flexural parameter value, a well-fit gravity model with similar α value to the topo model and a reasonable ρ_0 value could reduce the 10% α range to within acceptable limits in the combined topograv model (see profiles 10 and 96). A primary asset of a joint topography-gravity minimization scheme with misfit, wavelength sensitivity, and density contrast quality criteria is that it limits acceptable model fits to those for which the flexural parameter and amplitude are consistent for both the topography and gravity data sets. The

parameter sets obtained by simultaneous modeling are therefore more suitable for depth, moment and mechanical thickness analysis than those obtained by modeling topography and gravity alone.

Discussion

Depth Versus Age

The value of d_0 , the depth at the first zero crossing, should be approximately zero, assuming a perfect age correction. The mean value of d_0 is approximately +112 m with a standard deviation of about 268 m for the topo and topograv modeling schemes. Furthermore, there is no apparent age relation for the depth parameter (correlation coefficient of 0.17). Thus the *Parsons and Sclater* [1977] age correction has adequately and unbiasedly corrected the depth at least with respect to the DC offset. The low degree of slope evident in the vast majority of profiles further affirms that age related tilt has, for the most part, been adequately corrected. These depth versus age results are shown in Figure 7 (after adding the previously subtracted PSM depth) where we have plotted the modeled ocean depth at each trench-outer rise versus the age of the seafloor at the first

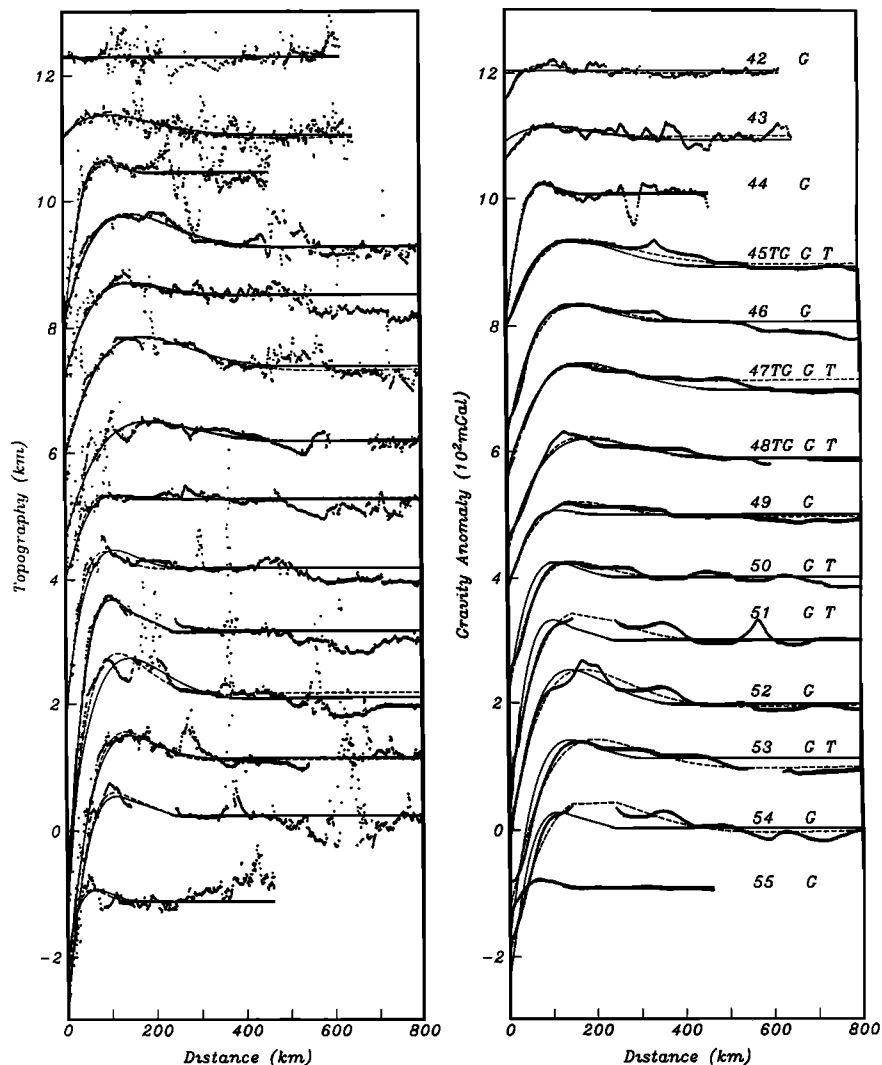


Figure 5. (continued)

zero crossing seaward of the trench axis. Also shown are depth versus age relations predicted by the *Parsons and Sclater* [1977] plate cooling model (PSM, solid curve), the half-space cooling model (HS, dashed curve) and the GDH1 model (dotted curve) of *Stein and Stein* [1992] (i.e., a plate-cooling model having a hot and thin lithosphere). For ages less than 70 Ma the data are equally scattered about all of the models. In many cases the estimated depth is less than all model depths; this bias is to be expected since we have not accounted for sediment loading. Between 80 and 100 Ma the PSM model fits best, while between 110 and 130 Ma the GDH1 model fits best. One advantage of our analysis over previous depth versus age studies is that since we model the trench/outer rise signature, we are able to estimate seafloor depth on very old seafloor near the trench axis. Several of our estimates are for 130 Ma seafloor where we find that the PSM model fits better than the GDH1 model; a sediment correction would increase the depth estimates and improve the fit to the PSM curve. Next, we show that the lithosphere of the GDH1 model is too hot and thin to maintain the bending moment needed to support the observed outer rise topography at older subduction zones (> 100 Ma).

Bending Moment Versus Age

The flexural amplitude (w_o) values for the three modeling schemes range from several hundred to several thousand meters. For comparisons with previous studies [*Caldwell et al.*, 1976; *Caldwell and Turcotte*, 1979; *Jones et al.*, 1978; *Turcotte et al.*, 1978], the theoretical elastic plate relation between the amplitude parameter w_o and the nominal height of the outer bulge w_b is

$$w_o = \sqrt{2} \exp\left(\frac{\pi}{4}\right) w_b \cong 3.10 w_b . \quad (10)$$

Usually, the model amplitude values w_o and the values obtained by visual inspection of the profiles w_b roughly correspond after scaling. Also, our values generally conform to those obtained by the previous studies at the same trenches. However, it should be noted that visual estimates of w_b are very sensitive to the value of reference depth d_o used. In many previous studies [*Caldwell et al.*, 1976; *Caldwell and Turcotte*, 1979; *Jones et al.*, 1978; *Turcotte et al.*, 1978; *Judge and McNutt*, 1991], d_o was chosen visually prior to flexural

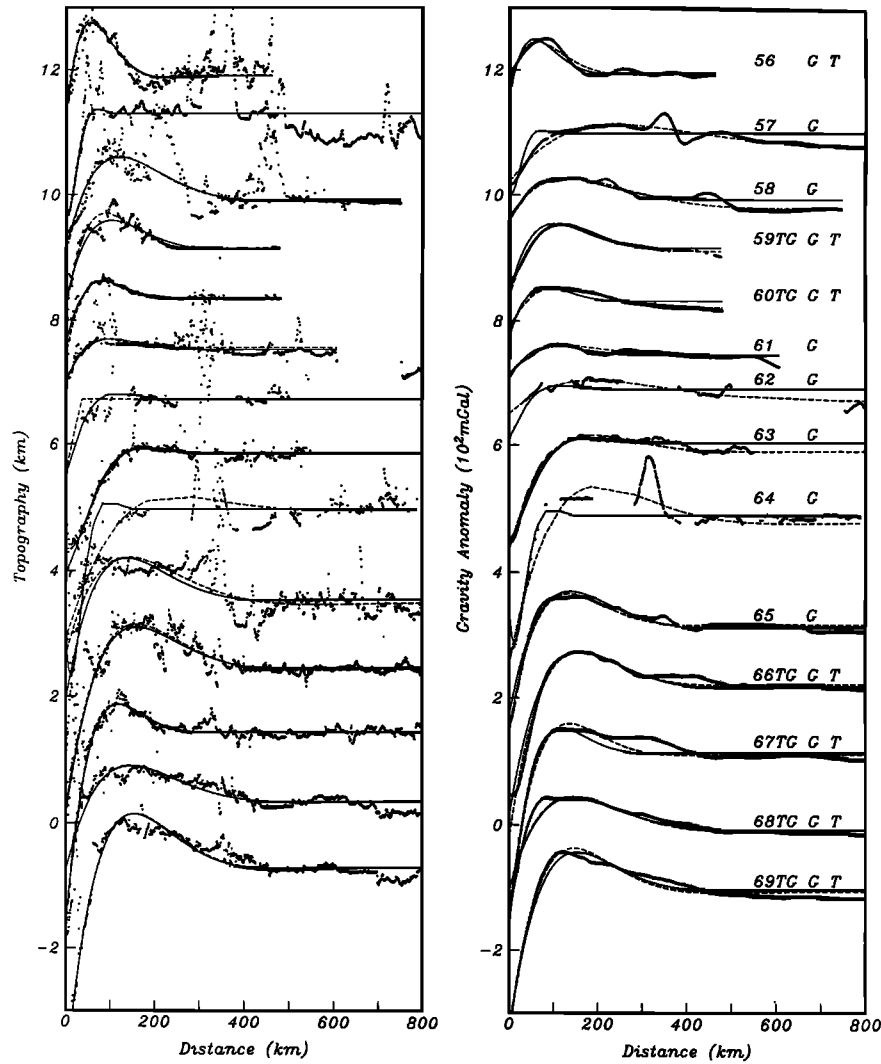


Figure 5. (continued)

modeling. We believe our misfit method is better because w_0 and d_0 are estimated simultaneously.

As noted by *Goetze and Evans* [1979], the bending moment needed to support the outer rise can be estimated by simply integrating the excess topography times the mantle/water density contrast ρ_0 times the moment arm:

$$M(x_0) = \int_{x_0}^{\infty} w(x) \rho_0 (x - x_0) dx, \quad (11)$$

where $w(x)$ is the excess topography and x_0 is the location of the moment. Although, in theory, a model fit is not needed to estimate this moment, topographic noise causes this integral to be unstable. The thin elastic plate flexure model provides a smooth fit to the observations that can easily be integrated to estimate the moment at x_0 :

$$M_0 = \frac{\rho_0 g}{2} \alpha^2 w_0, \quad (12)$$

where ρ_0 is set to 2200 kg m^{-3} .

A plot of this moment (for topograv) for the 37 trench profiles that pass all three editing criteria versus age is shown in Figure 8. Bending moment values are presented in Table 1

together with their associated curvature (K_0) values (see (2)). For ages less than 60 Ma, in the Middle America, Peru, Chile, and Aleutian Trenches, the bending moments are, in most cases, less than 10^{17} N and at greater ages, bending moments have a wide range up to a maximum of $3 \times 10^{17} \text{ N}$. This maximum bending moment provides an upper limit on the overall strength of the oceanic lithosphere in response to bending [*Turcotte et al.*, 1978; *Goetze and Evans*, 1979]. Our results are in general agreement with previous studies which show a rapid increase in maximum bending moment with increasing age [*McNutt and Menard*, 1982; *McAdoo et al.*, 1985]. However, our study uses a much larger data set and spans a much wider range than previously reported. These bending moment data can be used to constrain models of the thermal and mechanical properties of the oceanic lithosphere.

At high curvatures, the large fiber stresses cause brittle failure and ductile flow in the upper and lower lithosphere, respectively. The lithosphere is said to be moment saturated when the plate continues to bend without an increase in applied moment; it is nearly moment saturated when the curvature of the plate exceeds about $5 \times 10^{-7} \text{ m}^{-1}$. The vast majority of our model profiles exhibit curvatures which exceed

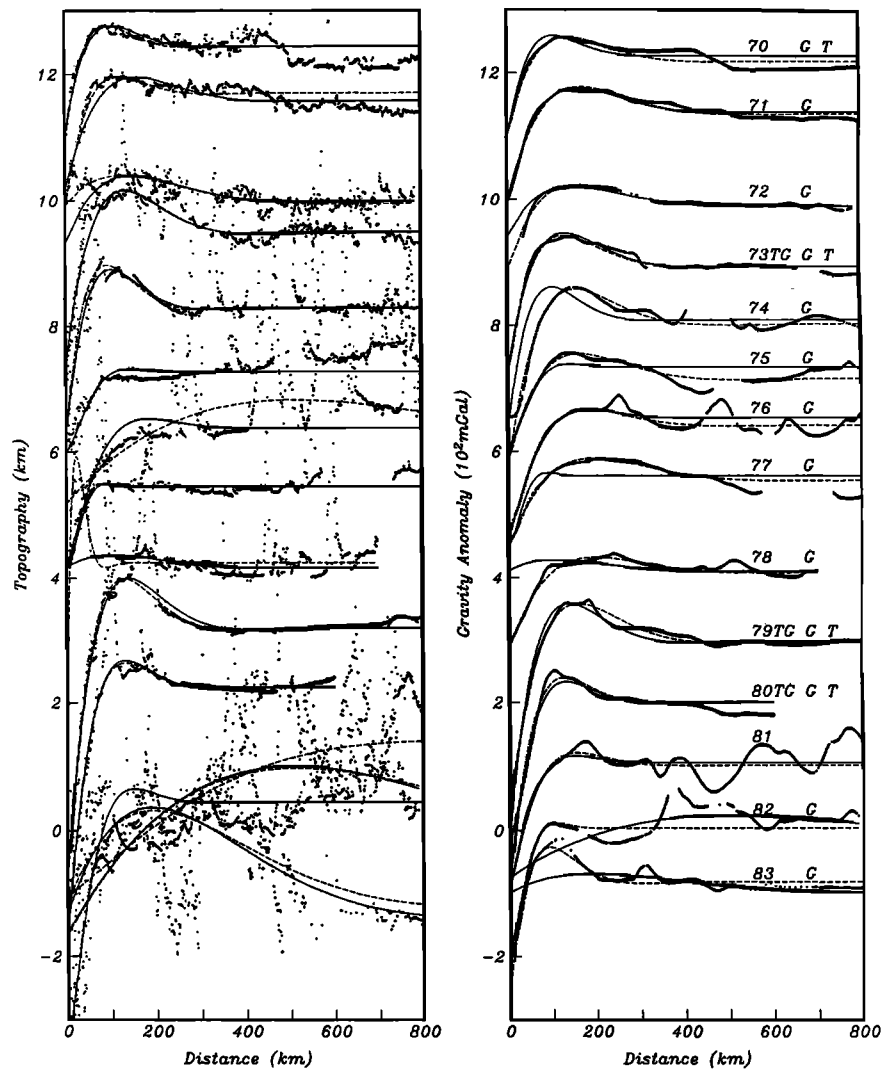


Figure 5. (continued)

10^{-7} m^{-1} , and many are moment saturated (Table 1). Thus these near-maximum moments can be compared with theoretical maximum moments calculated from models of lithospheric strength versus depth. To estimate these saturation moments, we used the yield strength envelope formulation of *Brace and Kohlstedt* [1980] with zero pore pressure and a dry olivine rheology from *Kirby* [1983]. This combination provides a maximum strength lithosphere for a given thermal profile. At a given lithospheric age the temperature versus depth profile was calculated for three models, the *Parsons and Sclater* [1977] cooling plate (PSM) and half-space (HS) model and the GDH1 model of *Stein and Stein* [1992]. We calculated the yield strength versus depth for both tension and compression and then imposed a stress versus depth profile corresponding to a large curvature with zero horizontal, inplane end load. After limiting the imposed stress to be less than the yield stress envelope, the depth of the nodal stress was adjusted iteratively so the end load was zero. The final saturation bending moment is

$$M = \int_0^h \Delta\sigma(z - z_n) dz, \quad (13)$$

where $\Delta\sigma$ is the deviatoric stress, z is depth, z_n is the nodal

stress depth, and h is the plate thickness. Saturation bending moments versus age for each of the three thermal models are plotted in Figure 8 along with the moments estimated from the profiles. The observed bending moments should not exceed the saturation bending moment. Except for three estimates between 24 and 45 Ma both the HS and the PSM models provide an upper bound on the observations. In contrast, about one half of the observed moments in the 120-150 Ma age range exceed the GDH1 model. We conclude that the lithosphere of the GDH1 model is too hot and thin to maintain the observed outer rises seaward of many subduction zones, especially outer rises on older lithosphere (> 100 Ma).

Mechanical Thickness Versus Age

The flexural parameter α displays a positive age correlation (Figure 6), particularly with respect to the gravity parameter set. Best estimates of α are used to calculate the corresponding effective elastic thickness (Table 1) using (4). Unlike most previous studies [*Caldwell et al.*, 1976; *Caldwell and Turcotte*, 1979; *Carey and Dubois*, 1981; *Jones et al.*, 1978; *McAdoo et al.*, 1978], our individual estimates of h_e have considerable scatter and do not constrain a particular isotherm increasing as

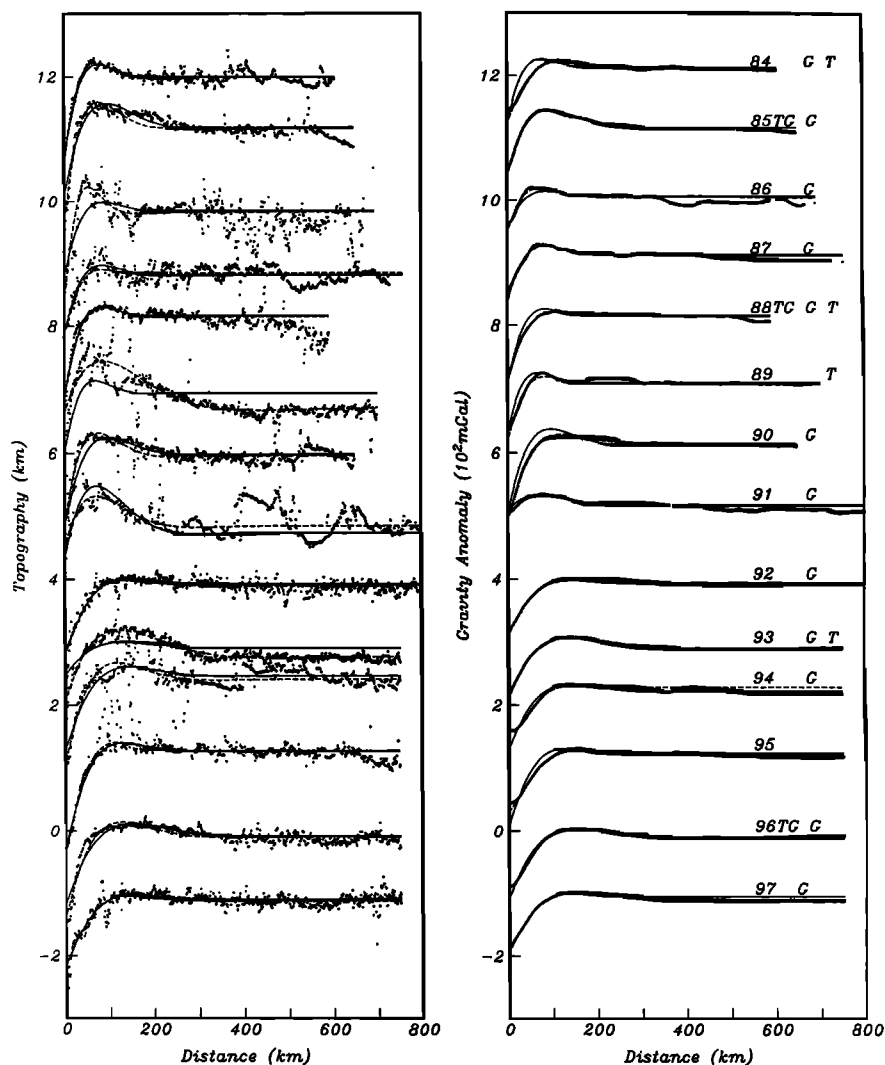


Figure 5. (continued)

the square root of age. The scatter is not likely to be caused by the utilization of a combined modeling scheme since there is substantial scatter within the topo and grav best fit α values. Nevertheless, these values agree, in general, with the compiled list presented in Table 1c of Wessel [1992], particularly for the topo modeling scheme ($\lambda = 0$), with noteworthy exceptions of the Aleutian Trench, for which our values are lower, and the Kuril Trench, for which our values are higher. We believe the scatter in our results and the poor agreement with the simple square root of age increase reflects uncertainties inherent in estimating flexure parameters, such as bathymetric noise and non flexural topography [McQueen and Lambeck, 1989] as well as inelastic bending and accumulated thermoelastic stress [Wessel, 1992].

As discussed in the previous section, the moderate-high curvatures observed for a majority of profiles indicate that a significant proportion of the plate is behaving inelastically. For these trenches, the true mechanical thickness (i.e., the depth to the nominal isotherm where materials are no longer capable of sustaining stress over geologic periods) is greater than the elastic thickness estimate. Following McNutt and Menard [1982], mechanical thickness estimates are obtained from the elastic thickness and curvature. According to S.

Mueller and R. J. Phillips (unpublished manuscript, 1992), using this conversion method with curvatures obtained at the first zero crossing of the best fitting elastic profile results in an underestimation of the mechanical thickness by 10% for 50 Ma lithosphere and by 8% for lithosphere older than 90 Ma. This error does not exceed 10% even at near-full saturation.

The variation of mechanical thickness estimates (Table 1), for topograv, with age is shown in Figure 9 along with mechanical thickness-age curves (750° isotherm) obtained by the half-space (HS), plate (PSM), and GDH1 models. Mechanical thickness increases rapidly over the age range of 10 to 60 Ma and then flattens over the range 80 to 150 Ma. While mechanical thickness estimates appear to confirm that lithospheric cooling results in thickening of the mechanical lithosphere with age, the wide scatter of the data do not allow for discrimination between the three thermal models, or even the determination of the isotherm which may define the base of the lithosphere.

Limitations of the Modeling

The high scatter exhibited by the flexural parameter, effective elastic thickness and mechanical thickness values

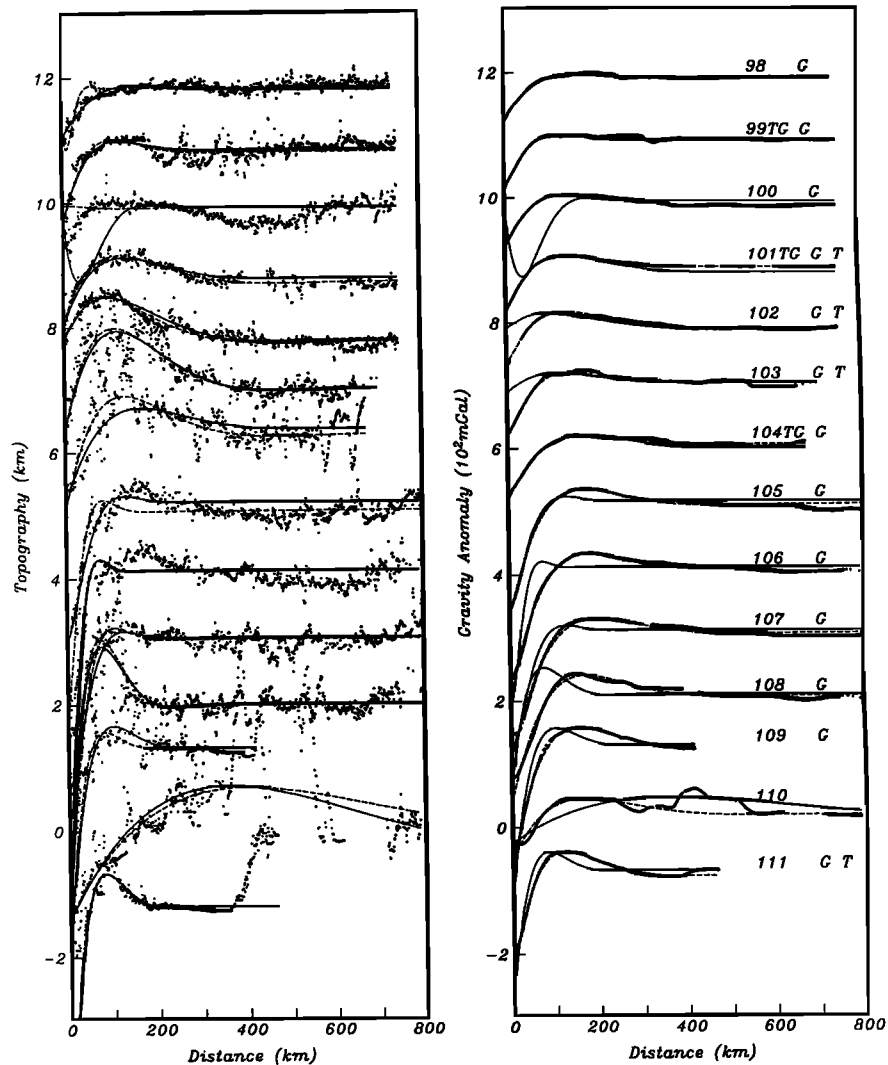


Figure 5. (continued)

highlights the limitations of trench flexural modeling. According to *Wessel* [1992], the underlying problem with h_m versus age data is that the estimated quantities have far more degrees of freedom than lithospheric age alone. At trenches, complications due to inelastic processes, inplane stress, unbending history and thermal stress history cannot be constrained adequately and are affected by unknown factors such as vertically integrated rheology, load size, local and regional stress history and thermal history.

Curvature-induced inelastic processes result in progressive failure in the plate and a variable flexural rigidity throughout a given profile. Though our profiles were adequately fit by a simple elastic model, several profiles exhibited fits with a systematic error. For example, in profile 68, the landward slope from the outer bulge is steeper than the model predicts, whereas the seaward slope is more gradual than the model predicts, implying that rigidity is diminished as the plate migrates across the outer rise. According to *Judge and McNutt* [1991], values of elastic thickness found by assuming constant rigidity along profiles can be considered weighted averages of the true elastic thickness along the length of the profile. Our flexural rigidity and effective elastic thickness data correspond closely to the values near the trench and outer rise due to our fitting-weighting scheme. Nevertheless,

curvatures obtained by *Judge and McNutt* [1991] using variable rigidity were approximately 1.6 times the curvatures calculated assuming constant rigidity. Therefore our h_m values may underestimate the true mechanical thickness for high curvature profiles where inelastic processes result in variable rigidity.

Regional in-plane stress, both compressive [*Bodine and Watts*, 1979] at the Bonin Trench and Southern Marianas Trench and tensile [*Judge and McNutt*, 1991] at the Peru Trench and Chile Trench, has been invoked to explain flexure and seismicity observations. S. Mueller and R. J. Phillips (unpublished manuscript, 1992) fit elastic models to synthetic profiles with various inplane stress histories and were unable to recover the appropriate value of inplane stress. Moreover, the imposition of compressive stress before and after bending did not change the effective elastic thickness determined, though 5 km uncertainty was introduced. Conversely, regional tension tended to make lithosphere appear substantially weaker and thinner. Unfortunately, regional stress fields in the vicinity of trench flexure are still poorly constrained by intraplate focal mechanisms [*Wiens and Stein*, 1984; *Bergman and Solomon*, 1984; *Bergman*, 1986].

Wessel [1992], in an effort to explain the bimodal nature of h_m versus age data at seamounts and trenches, evaluated the combined effects of flexural bending stresses and thermal

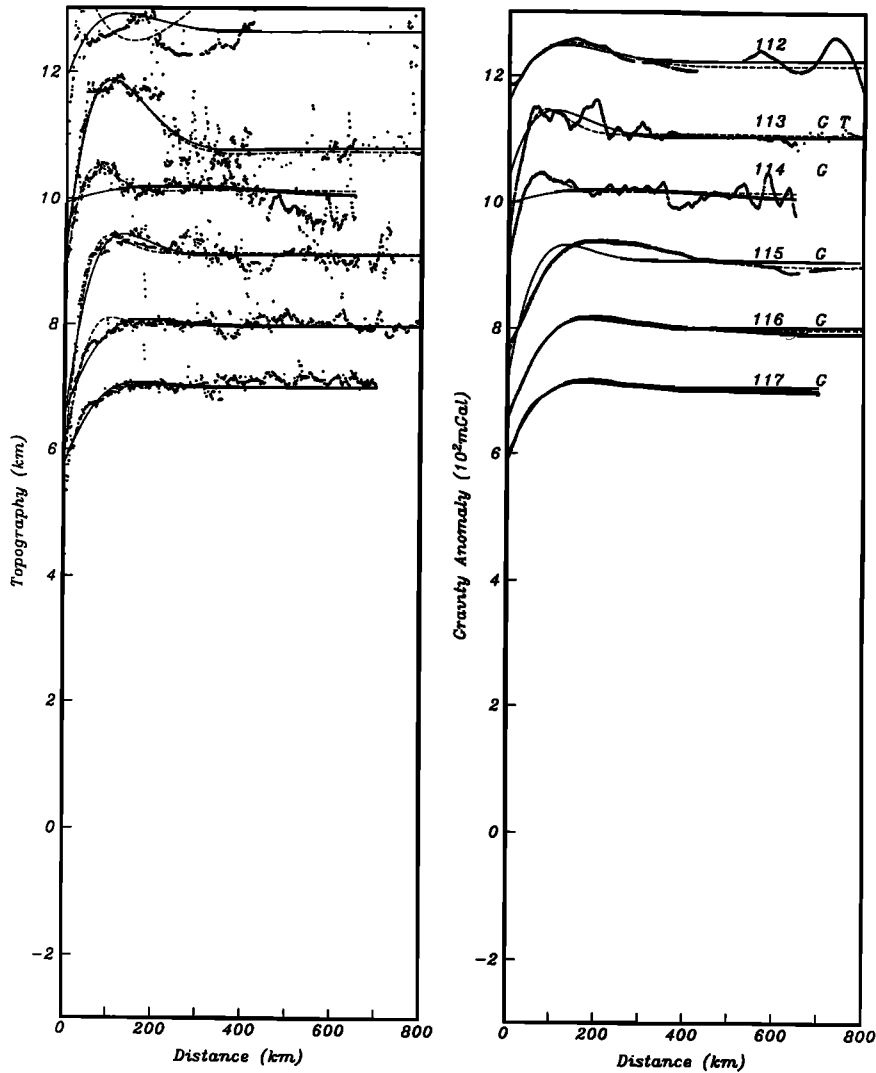


Figure 5. (continued)

bending stresses due to depth-dependent, temporally integrated cooling of the lithosphere. Constructive interference beneath seamounts drives the plate to premature failure, therefore giving the impression of a relatively weaker plate. Conversely, thermal stresses at trenches are largely relieved by the opposite flexural bending stresses and the plate appears to be stronger [Wessel, 1992]. The result of this stress superposition for 30 Ma lithosphere is a 5-20% overestimation of h_e at trenches and a 10-40% underestimation of h_e at seamounts for curvatures less than 4×10^{-7} . Wessel [1992, Figure 12b] provides bias estimates for trenches and seamounts over a range of ages and curvatures. Approximately 10 profiles in the present study suggest an overestimation bias which exceeds 10% (Figure 9). Notably, profiles 10 (Aleutians), 96, and 101 (Peru), which lie significantly above the general h_m trend at 30-50 m.y., are lowered by about 30%, back to the expected value. The corrected mechanical thicknesses demonstrate an approximate $\text{age}^{1/2}$ correlation, though substantial scatter still prohibit resolution of the best fitting lithospheric basal isotherm model.

Conclusions

A global survey of trench profiles, from depth soundings and satellite gravity grid data, demonstrates that the majority

of subducting plate profiles contain an outer rise, in response to a bending moment applied by the subducted plate. These profiles can be quantitatively fit, after high-resolution age correction, using a simple elastic model with no required tilt. A modeling scheme which simultaneously fits gravity and topography is utilized to exclude models which poorly constrain the flexural parameter and flexural amplitude due to nonflexural deformation in topographic modeling and deep structure in gravity. In accordance with previous investigations, elastic thickness values exhibit a discrepancy between topographic and gravitational modeling values; gravitational elastic thicknesses exceed those obtained by topographic modeling. Parameter values obtained from a combined data set fitting scheme, are selected for goodness of fit, sensitivity of fit to the flexural parameter and approximate noncompensation. A primary attribute of the combined topography-gravity modeling scheme is that the best fitting models are restricted to those for which the flexural parameter and amplitude are consistent for both the topography and gravity data sets.

The value of the depth parameter at the first zero crossing was obtained from the modeling procedure, yielding depth determinations at the oldest possible location prior to subduction. Though we have not accounted for sediment loading, we find that between 80 and 100 Ma and 135-145 Ma

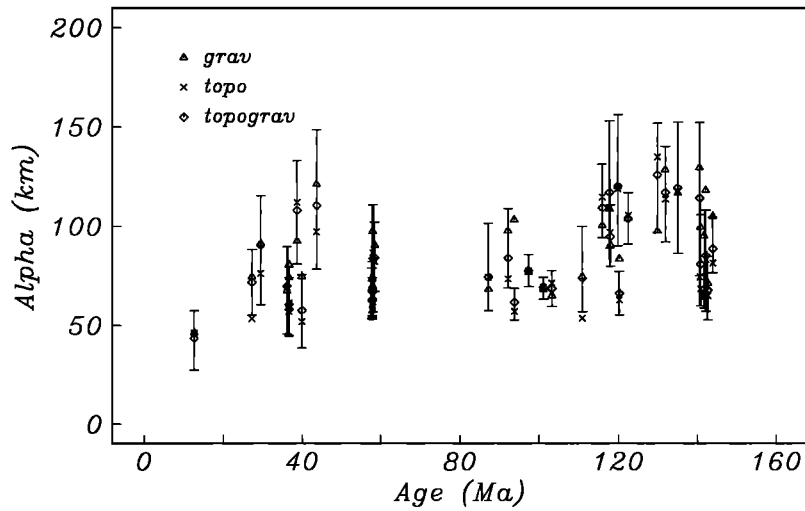


Figure 6. Flexural parameter (α) estimates for the topograv ($\lambda = 0.4$), grav ($\lambda = \infty$), and topo ($\lambda = 0$) values which correspond to the 37 "successfully fit" topograv models with respect to model ages at the first zero crossing from a two-dimensional interpolation of an age grid [Roest *et al.*, 1992]. Error bars correspond to the 10% misfit ranges for the topograv modeling scheme.

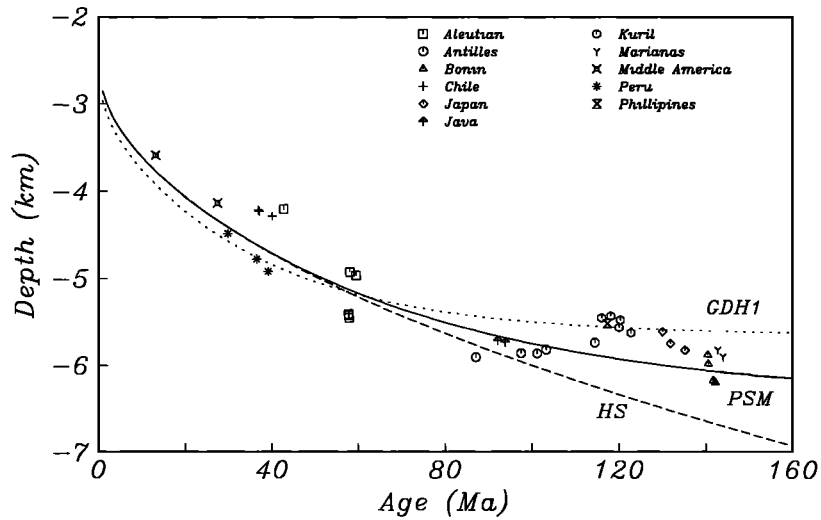


Figure 7. Best fit model depths at the first zero crossing with respect to model ages at the first zero crossing from a two-dimensional interpolation of an age grid [Roest *et al.*, 1992], with predicted depths according to the HS (dashed), PSM (solid), and GDH1 (dotted) thermal models. See key on figure for trench symbols.

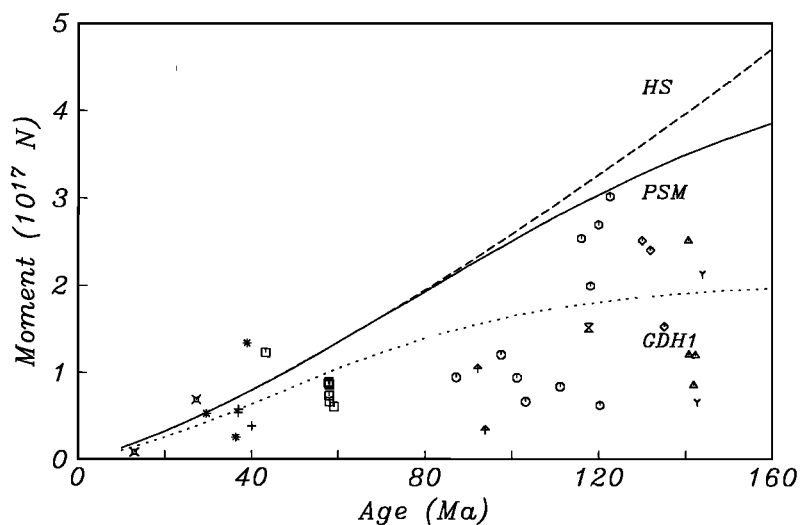


Figure 8. Bending moment values determined using the thin elastic plate model (equation (12)) with respect to model ages at the first zero crossing from a two-dimensional interpolation of an age grid [Roest *et al.*, 1992], with saturation moments predicted according to the HS (dashed), PSM (solid), and GDH1 (dotted) thermal models. Trench symbol assignment is identical to Figure 7.

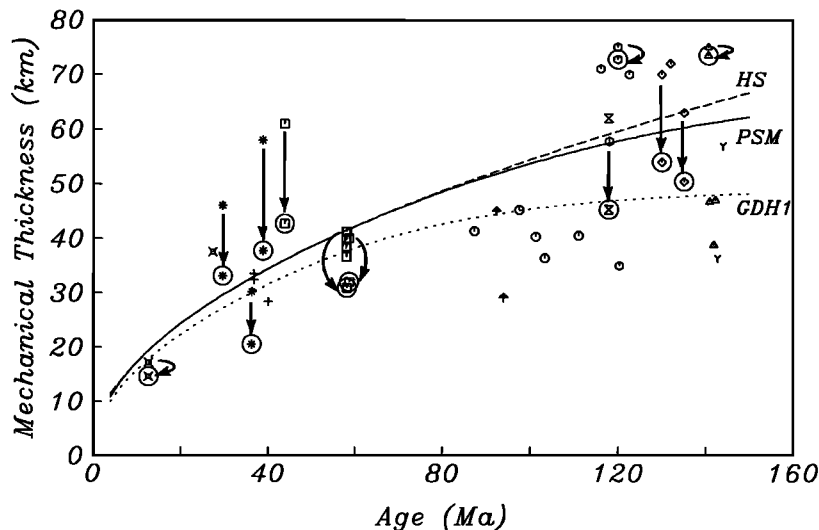


Figure 9. Mechanical thicknesses determined using the h_e to h_m conversion method proposed by McNutt and Menard [1982] with respect to model ages at the first zero crossing from a two-dimensional interpolation of an age grid [Roest *et al.*, 1992], with predicted model thicknesses according to the HS (dashed), PSM (solid), and GDH1 (dotted) thermal models with base depth corresponding to the 750° isotherm. Trench symbol assignment is identical to Figure 7. Circled points correspond to values corrected for thermal stress bias [Wessel, 1992].

the PSM model fits best, while between 110 and 130 Ma the GDH1 model fits best. A sediment correction would further establish the superior fit of the PSM over the GDH1 model to the depth parameter.

The moderate and high curvatures present at a majority of profiles imply that a substantial component of stress relief is occurring by inelastic processes so that the effective elastic thickness values substantially underestimate the true mechanical thickness. Bending moments calculated at the first zero crossing were compared with the saturation moment predicted by the half-space and plate cooling models of Parsons and Sclater [1977] and the GDH1 model of Stein and Stein [1992]. Since approximately one half of the observed moments at trenches older than 120 Ma exceeded the saturation moment, we conclude that the GDH1 lithosphere is too hot and thin to maintain the observed outer rises seaward of many subduction zones. Mechanical thickness estimates were obtained from the elastic thickness and curvature values but scatter in the data, due to bathymetric noise and poor constraint of complicating factors (inplane stress, unbending history, and remnant thermal stress), precludes discrimination between the half-space, plate, and GDH1 cooling models.

Acknowledgments. We thank the associate editor and the referees, David McAdoo and Herbert McQueen, for their careful and constructive reviews of the original manuscript. Walter Smith and Pal Wessel provided useful advice regarding the use of GMT and the significance of yield strength envelopes and thermal stresses, respectively. We thank Catherine Johnson and Andrew Goodwillie for important insights and suggestions regarding conceptual and technical matters. Daniel Levitt was supported by an NSF Graduate Fellowship. Additional support was provided by the NASA Venus Data Analysis Program NAGW-3503 and the NSF MG&G Program OCE-9217164.

References

Bergman, E. A., Intraplate earthquakes and the state of stress in oceanic lithosphere, *Tectonophysics*, 132, 1-35, 1986.

- Bergman, E. A., and S. C. Solomon, Source mechanisms of earthquakes near mid-ocean ridges from body waveform inversion: Implications for the early evolution of oceanic lithosphere, *J. Geophys. Res.*, 89, 11,415-11,441, 1984.
- Bodine, J. H., and A. B. Watts, On lithospheric flexure seaward of the Bonin and Mariana trenches, *Earth Planet. Sci. Lett.*, 43, 132-148, 1979.
- Brace, W. F., and D. L. Kohlstedt, Limits on lithospheric stress imposed by laboratory experiments, *J. Geophys. Res.*, 85, 6248-6252, 1980.
- Caldwell, J. G., and D. L. Turcotte, Dependence of the thickness of the elastic oceanic lithosphere on age, *J. Geophys. Res.*, 84, 7572-7576, 1979.
- Caldwell, J. G., W. F. Haxby, D. E. Karig, and D. L. Turcotte, On the applicability of a universal elastic trench profile, *Earth Planet. Sci. Lett.*, 31, 239-246, 1976.
- Carey, E., and J. Dubois, Behavior of the oceanic lithosphere at subduction zones: Plastic yield strength from a finite-element method, *Tectonophysics*, 74, 99-110, 1981.
- Carter, D. J. T., *Echo Sounding Correction Tables: Formerly Matthews' Tables*, 150 pp., Hydrographic Department, Ministry of Defense, Taunton, Somerset, England, 1980.
- Cochran, J. R., Variations in subsidence rates along intermediate and fast spreading mid-ocean ridges, *Geophys. J. R. Astron. Soc.*, 87, 421-459, 1986.
- DeBremackeer, J. C., Is the oceanic lithosphere elastic or viscous?, *J. Geophys. Res.*, 82, 2001-2004, 1977.
- Goetze, C., and B. Evans, Stress and temperature in the bending lithosphere as constrained by experimental rock mechanics, *Geophys. J. R. Astron. Soc.*, 59, 463-478, 1979.
- Gunn, R., A quantitative evaluation of the influence of the lithosphere on the anomalies of gravity, *J. Franklin Inst.*, 236, 373-396, 1943.
- Hayes, D. E., Age-depth relationships and depth anomalies in the Southeast Indian Ocean and South Atlantic Ocean, *J. Geophys. Res.*, 93, 2937-2954, 1988.
- Jones, G. M., T. W. C. Hilde, G. F. Sharman, and D. C. Agnew, Fault patterns in outer trench walls and their tectonic significance, *J. Phys. Earth*, 26, S85-S101, 1978.
- Judge, A.V., and M. K. McNutt, The relationship between plate curvature and elastic plate thickness: A study of the Peru-Chile trench, *J. Geophys. Res.*, 96, 16,625-16640, 1991.
- Kirby, S. H., Rheology of the lithosphere, *Rev. Geophys.*, 21, 1458-1487, 1983.

- Marty, J. C., and A. Cazenave, Regional variations in subsidence rate of oceanic plates: A global analysis, *Earth Planet. Sci. Lett.*, *94*, 301-315, 1989.
- Mathworks, Matlab: High-performance numeric computation and visualization software, report, Natick, Mass., 1993.
- McAdoo, D. C., and C. F. Martin, Seasat observations of lithospheric flexure seaward of trenches, *J. Geophys. Res.*, *89*, 3201-3210, 1984.
- McAdoo, D. C., J. G. Caldwell, and D. L. Turcotte, On the elastic-perfectly plastic bending of the lithosphere under generalized loading with application to the Kuril Trench, *Geophys. J. R. Astron. Soc.*, *54*, 11-26, 1978.
- McAdoo, D. C., C. F. Martin, and S. Poulou, Seasat observations of flexure: Evidence for a strong lithosphere, *Tectonophysics*, *116*, 209-222, 1985.
- McKenzie, D. P., Some remarks on heat flow and gravity anomalies, *J. Geophys. Res.*, *72*, 6261-6273, 1967.
- McNutt, M. K., Lithospheric flexure and thermal anomalies, *J. Geophys. Res.*, *89*, 11,180-11,194, 1984.
- McNutt, M. K., and H. W. Menard, Constraints on yield strength in the oceanic lithosphere derived from observations of flexure, *Geophys. J. R. Astron. Soc.*, *71*, 363-394, 1982.
- McQueen, H. W. S., and K. Lambeck, The accuracy of some lithospheric bending parameters, *Geophys. J.*, *96*, 401-413, 1989.
- Molnar, P., and T. Atwater, Interarc spreading and cordilleran tectonics as alternates related to the age of subducted oceanic lithosphere, *Earth Planet. Sci. Lett.*, *41*, 330-340, 1978.
- Nelder, J. A., and R. Mead, A simplex method for function minimization, *Comput. J.*, *7*, 308-313, 1965.
- Neumann, G. A., D. W. Forsyth, and D. T. Sandwell, Comparison of marine gravity from shipboard and high-density satellite altimetry along the Mid-Atlantic Ridge, 30.5-35.5°S, *Geophys. Res. Lett.*, *20*, 1639-1642, 1993.
- Parsons, B., and P. Molnar, The origin of outer topographic rises associated with trenches, *Geophys. J. R. Astron. Soc.*, *45*, 707-712, 1976.
- Parsons, B., and J. G. Sclater, An analysis of the variation of oceanic floor bathymetry and heat flow with age, *J. Geophys. Res.*, *82*, 803-827, 1977.
- Roest, W. R., R. D. Mueller, J.-Y. Royer, and L. M. Gahagan, A high resolution digital age map of the world's oceans, *Eos Trans. AGU*, *73* (43), Fall Meeting suppl., 586, 1992.
- Sandwell, D. T., Along-track deflection of the vertical from Seasat: GEBCO overlays, *NOAA Tech. Memo., NOS NGS-40*, 8 pp., 1984.
- Sandwell, D. T., Antarctic marine gravity field from high-density satellite altimetry, *Geophys. J. Int.*, *109*, 437-448, 1992.
- Sandwell, D. T., and M. B. Ruiz, Along-track gravity anomalies from Geosat and Seasat altimetry: GEBCO Overlays, *Mar. Geophys. Res.*, *14*, 165-227, 1992.
- Sandwell, D. T., and W. H. F. Smith, global marine gravity from ERS-1, Geosat, and Seasat reveals new tectonic fabric, *Eos Trans. AGU*, *73* (43), Fall Meeting suppl., 133, 1992.
- Smith, W. H. F., On the accuracy of digital bathymetric data, *J. Geophys. Res.*, *98*, 9591-9603, 1993.
- Stein, C. A., and S. Stein, A model for the global variation in oceanic depth and heat flow with lithospheric age, *Nature*, *359*, 123-129, 1992.
- Turcotte, D. L., Flexure, *Adv. Geophys.*, *21*, 51-86, 1979.
- Turcotte, D. L., and E. R. Oxburgh, Finite amplitude convection cells and continental drift, *J. Fluid Mech.*, *28*, 29-42, 1967.
- Turcotte, D. L., and G. Schubert, *Geodynamics: Applications of Continuum Physics to Geological Problems*, John Wiley, New York., 1982.
- Turcotte, D. L., D. C. McAdoo, and J. G. Caldwell, An elastic-perfectly plastic analysis of the bending of the lithosphere at a trench, *Tectonophysics*, *47*, 193-205, 1978.
- Watts, A. B., An analysis of isostasy in the world's oceans, 1, Hawaiian-Emperor seamount chain, *J. Geophys. Res.*, *83*, 5989-6004, 1978.
- Wessel, P., Thermal stress and the bimodal distribution of elastic thickness estimates of the oceanic lithosphere, *J. Geophys. Res.*, *97*, 14,177-14,193, 1992.
- Wessel, P., and W. H. F. Smith, Free software helps map and display data, *Eos Trans. AGU*, *72*, 441-446, 1991.
- Wiens, D. A., and S. Stein, Intraplate seismicity and stresses in young oceanic lithosphere, *J. Geophys. Res.*, *89*, 11,442-11,464, 1984.

D. A. Levitt and D. T. Sandwell, Scripps Institution of Oceanography, 9500 Gilman Drive, La Jolla, CA 92093-0225.

(Received September 28, 1993; revised September 1, 1994; accepted September 13, 1994.)